

# OISTER Optical and Near-Infrared Observations of the Super-Chandrasekhar Supernova Candidate SN 2012dn: Dust Emission from the Circumstellar Shell

Masayuki YAMANAKA<sup>1,2</sup>, Keiichi MAEDA<sup>3,4</sup>, Masaomi TANAKA<sup>5</sup>, Nozomu TOMINAGA<sup>1,4</sup>, Koji S. KAWABATA<sup>6,7</sup>, Katsutoshi TAKAKI<sup>7</sup>, Miho KAWABATA<sup>7</sup>, Tatsuya NAKAOKA<sup>7</sup>, Issei UENO<sup>7</sup>, Hiroshi AKITAYA<sup>6,7</sup>, Takahiro NAGAYAMA<sup>8,9</sup>, Jun TAKAHASHI<sup>10</sup>, Satoshi HONDA<sup>10</sup>, Toshihiro OMODAKA<sup>9</sup>, Ryo MIYANOSHITA<sup>9</sup>, Takashi NAGAO<sup>3</sup>, Makoto WATANABE<sup>11</sup>, Mizuki ISOGAI<sup>5,12</sup>, Akira ARAI<sup>10,12</sup>, Ryosuke ITOH<sup>7</sup>, Takahiro UI<sup>7</sup>, Makoto UEMURA<sup>6,7</sup>, Michitoshi YOSHIDA<sup>6,7</sup>, Hidekazu HANAYAMA<sup>13</sup>, Daisuke KURODA<sup>14</sup>, Nobuharu UKITA<sup>14</sup>, Kenshi YANAGISAWA<sup>14</sup>, Hideyuki IZUMIURA<sup>14</sup>, Yoshihiko SAITO<sup>15</sup>, Kazunari MASUMOTO<sup>16</sup>, Rikako ONO<sup>16</sup>, Ryo NOGUCHI<sup>16</sup>, Katsura MATSUMOTO<sup>16</sup>, Daisaku NOGAMI<sup>2,3</sup>, Tomoki MOROKUMA<sup>17</sup>, Yumiko OASA<sup>18</sup>, and Kazuhiro SEKIGUCHI<sup>5</sup>.

<sup>1</sup>Department of Physics, Faculty of Science and Engineering, Konan University, Okamoto, Kobe, Hyogo 658-8501, Japan; yamanaka@center.konan-u.ac.jp

<sup>2</sup>Kwasan Observatory, Kyoto University, 17-1 Kitakazan-ohmine-cho, Yamashina-ku, Kyoto, 607-8471, Japan

<sup>3</sup>Department of Astronomy, Graduate School of Science, Kyoto University, Sakyo-ku, Kyoto 606-8502, Japan

<sup>4</sup>Kavli Institute for the Physics and Mathematics of the Universe (WPI), The University of Tokyo, 5-1-5 Kashiwanoha, Kashiwa, Chiba 277-8583, Japan

<sup>5</sup>National Astronomical Observatory of Japan, Osawa, Mitaka, Tokyo 181-8588, Japan

<sup>6</sup>Hiroshima Astrophysical Science Center, Hiroshima University, Higashi-Hiroshima, Hiroshima 739-8526, Japan

<sup>7</sup>Department of Physical Science, Hiroshima University, Kagamiyama 1-3-1, Higashi-Hiroshima 739-8526, Japan

<sup>8</sup>Department of Astrophysics, Nagoya University, Chikusa-ku, Nagoya 464-8602, Japan

<sup>9</sup>Graduate School of Science and Engineering, Kagoshima University, 1-21-35 Korimoto, Kagoshima 890-0065, Japan

<sup>10</sup>Nishi-Harima Astronomical Observatory, Center for Astronomy, University of Hyogo, 407-2 Nishigaichi, Sayo-cho, Sayo, Hyogo 679-5313, Japan

<sup>11</sup>Department of Earth and Planetary Sciences, School of Science, Hokkaido University, Kita-ku, Sapporo 060-0810, Japan

<sup>12</sup>Koyama Astronomical Observatory, Kyoto Sangyo University, Motoyama, Kamigamo, Kita-Ku, Kyoto-City 603-8555, Japan

<sup>13</sup>Ishigakijima Astronomical Observatory, National Astronomical Observatory of Japan, 1024-1 Arakawa, Ishigaki, Okinawa 907-0024, Japan

<sup>14</sup>Okayama Astrophysical Observatory, National Astronomical Observatory of Japan, Honjo 3037-5, Kamogata, Asakuchi, Okayama 719-0232, Japan

<sup>15</sup>Department of Physics, Tokyo Institute of Technology, 2-12-1 Ookayama, Meguro-ku, Tokyo 152-8551, Japan

<sup>16</sup>Astronomical Institute, Osaka Kyoiku University, Asahigaoka, Kashiwara, Osaka 582-8582

<sup>17</sup>Institute of Astronomy, Graduate School of Science, The University of Tokyo, 2-21-1 Osawa, Mitaka, Tokyo 181-0015, Japan

<sup>18</sup>Faculty of Education, Saitama University, 255 Shimo-Okubo, Sakura, Saitama, 338-8570, Japan

Received ; Accepted

## Abstract

We present extensively dense observations of the super-Chandrasekhar supernova (SC SN) candidate SN 2012dn from  $-11$  to  $+140$  days after the date of its  $B$ -band maximum in the optical and near-infrared (NIR) wavelengths conducted through the OISTER ToO program. The NIR light curves and color evolutions up to 35 days after the  $B$ -band maximum provided an excellent match with those of another SC SN 2009dc, providing a further support to the nature of SN 2012dn as a SC SN. We found that SN 2012dn exhibited strong excesses in the NIR wavelengths from 30 days after the  $B$ -band maximum. The  $H$  and  $K_s$ -band light curves exhibited much later maximum dates at 40 and 70 days after the  $B$ -band maximum, respectively, compared with those of normal SNe Ia. The  $H$  and  $K_s$ -band light curves subtracted by those of SN 2009dc displayed plateaued evolutions, indicating a NIR echo from the surrounding dust. The distance to the inner boundary of the dust shell is limited to be  $4.8 - 6.4 \times 10^{-2}$  pc. No emission lines were found in its early phase spectrum, suggesting that the ejecta-CSM interaction could not occur. On the other hand, we found no signature that strongly supports the scenario of dust formation. The mass loss rate of the pre-explosion system is estimated to be  $10^{-6} - 10^{-5} M_{\odot} \text{ yr}^{-1}$ , assuming that the wind velocity of the system is  $10 - 100 \text{ km s}^{-1}$ , which suggests that the progenitor of SN 2012dn could be a recurrent nova system. We conclude that the progenitor of this SC SN could be explained by the single-degenerate scenario.

**Key words:** supernovae: general — supernovae: individual (SN 2012dn) — supernovae: individual (SNe 2009dc)

## 1 Introduction

Type Ia supernovae (SNe Ia) have been used to provide constraints on cosmological parameters through the use of their calibrated light curves (Riess et al. 1998; Perlmutter et al. 1999). Strong correlations exist between the rate of decline of the light curves and their absolute magnitudes (Phillips 1993; Phillips et al. 1999; Altavilla et al. 2004; Wang et al. 2006; Prieto et al. 2006; Folatelli et al. 2010). Homogeneous properties are thought to be reproduced by the similar masses of the progenitors (e.g., Branch et al. 1993, but see also Howell et al. 2006; Scalzo et al. 2010; Taubenberger et al. 2011 and therein). This would support a scenario that a thermonuclear runaway occurs at the center or off-center region of a white dwarf (WD), when it reaches the Chandrasekhar limiting mass ( $\sim 1.4M_{\odot}$ ) (Nomoto et al. 1984).

However, recently various observational outliers have been discovered, including overluminous SNe Ia (e.g., Super-Chandrasekhar SNe; Howell et al. 2006; Hicken et al. 2007;

Yamanaka et al. 2009; Tanaka et al. 2010; Yuan et al. 2010; Scalzo et al. 2010; Silverman et al. 2011; Taubenberger et al. 2011; Scalzo et al. 2012; Chakradhari et al. 2014), which represent a sub-class of SNe Ia studied in this paper. Super-Chandrasekhar SNe (SC SNe) have peculiar observational properties, e.g., an extremely high luminosity, slow rate of decline of the optical light curves, typically very slow expansion velocity, and anomalous carbon absorption features (Yamanaka et al. 2009; Silverman et al. 2011; Taubenberger et al. 2011). The large amount of the ejected  $^{56}\text{Ni}$  mass, as inferred from their peak luminosities, cannot be explained by the Chandrasekhar-limiting mass of the WD (Howell et al. 2006). Theoretical analysis of the light curves and spectra imply that the total ejected mass could significantly exceed the Chandrasekhar-limiting mass of a non-rotating WD and could even reach  $2.0\text{-}3.0M_{\odot}$  (Taubenberger et al. 2011; Hachinger et al. 2012; Kamiya et al. 2012), although an asymmetry of the ejecta without invoking the large  $^{56}\text{Ni}$  mass has also been discussed (Hillebrandt et al.

2007, but see Maeda & Iwamoto 2009; Tanaka et al. 2010).

Demonstrating the presence of circumstellar material (CSM) is critical for providing a constraint on the progenitor nature of an exploding star. The dense environment of the CSM could be formed by the shell being ejected through the mass loss from the companion star or through an optically thick wind arising from the WD. This is expected from a single-degenerate scenario (Nomoto 1982), while the environment surrounding two WDs would be scarce in a double-degenerate scenario (Iben & Tutukov 1984; Webbink 1984). Various possibilities for the existence of the CSM have been discussed, based on light echoes in the late-phase light curve mostly in the optical wavelength (Schaefer 1987; Sparks et al. 1999; Cappellaro et al. 2001; Patat 2005; Wang 2005; Patat et al. 2006; Quinn et al. 2006; Wang et al. 2008; Crotts 2015; Drozdov et al. 2015) and time-variable narrow absorption line systems for some SNe Ia (Patat et al. 2007; Simon et al. 2009). The stronger evidence of CSM has been reported for a class of SNe Ia-CSM showing a clear signature of the hydrodynamical interaction between the SN ejecta and the CSM (Hamuy et al. 2003; Dilday et al. 2012). We note that another important clue, a non-degenerate companion star, has been generally non-detected for normal SNe Ia either from the direct detection in pre-SN images (Li et al. 2011; Kelly et al. 2014) or the shock-heated early emission (Nugent et al. 2011; Yamanaka et al. 2014), while the possible signature has been reported for SN 2012cg (Marion et al. 2016). These various methods for detecting a companion star or CSM have not been applied to SC SNe to date.

Thermal emission from CS dust radiated by light originating from the central SN can also be detected in near-infrared (NIR) wavelength observations (Maeda et al. 2015) if CS dust is present. However, the geometrical structure of the progenitor system may affect the ability to detect such signatures. In any case, if the signatures of the CSM are acquired on subparsec scales, the nature of the progenitor should be limited to the single degenerate state.

SN 2012dn was discovered at a magnitude of 16.3 on Jul 13.3 (UT)<sup>1</sup> in the nearby galaxy, ESO 462-16 ( $\mu = 33.15$ ; Bock et al. 2012). Its spectrum resembled that of SC SN 2006gz at 10 days before maximum (Parrent & Howell 2012). Chakradhari et al. (2014) noted that the optical and ultraviolet properties of SN 2012dn are similar to those of SC candidate SN 2006gz. Therefore, SN 2012dn could be the nearest SC SN Ia candidate to date. Parrent et al. (2016) performed the detailed spectral analysis of SN 2012dn. They derived the ejected mass exceeding  $1.6M_{\odot}$ , indicating that SN 2012dn is a SC SN Ia. They also suggest that the origin of SN 2012dn might not be a merger event.

In this paper, we present intensively obtained samples of the optical and NIR observations of the super-

Chandrasekhar candidate SN 2012dn obtained through the Target-of-Opportunity (ToO) program in the Optical and Infrared Synergetic Telescopes for Education and Research (OISTER). We focus on the NIR data, which have never before been published. The NIR light curves and color exhibited strong excesses after  $t = 30$  d. The  $J$ ,  $H$ , and  $K_s$ -band fluxes were subtracted using the light curves of SN2009dc as a template. We demonstrate that the subtracted light curves could be naturally explained by dust echo models. The classification of SN 2012dn as a SC SN is also discussed using the NIR data. The nature of the progenitor system is then discussed using the mass loss rate and the distances to the CS dust shell derived from the dust echo model. Finally, we present our conclusion that a SC SN progenitor could originate from the single-degenerate scenario.

## 2 Observations and data reduction

Using the OISTER (Itoh et al. 2013; Itoh et al. 2014; Ishiguro et al. 2015; Kuroda et al. 2015; Yatsu et al. 2015; Yamanaka et al. 2015), ToO program, observations were conducted for SN 2012dn between  $t = -7$  and 140 d. Optical and NIR photometric observations of SN 2012dn were performed using different 10 telescopes, while spectroscopic observations were carried out using one telescope.

### 2.1 Optical photometry

We performed  $B$ ,  $V$ ,  $R$ ,  $I$ , and  $z' + Y$ -band photometric observations over 52 nights using the Hiroshima One-shot Wide-field Polarimeter (HOWPol; Kawabata et al. 2008) installed on the 1.5-m Kanata telescope,  $U$ ,  $B$ ,  $V$ ,  $R$ , and  $I$ -band observations on 44 nights with the Multi-spectral Imager (MSI; Watanabe et al. 2012) installed on the 1.6-m Pirka telescope, and  $B$ ,  $V$ ,  $I$ ,  $g'$ ,  $i'$ ,  $z'$ -band photometric observations over 24 nights with the Araki telescope Dual-band imager (Adler; Isogai et al. 2015) installed on the 1.3-m Araki telescope. The observatories, telescopes, and instruments participating in this program are summarized in Table 1.

We also performed  $g'$ ,  $R$ , and  $I$ -band observations using a robotic observation system, the Multicolor Imaging Telescopes for Survey and Monstrous Explosions (MITSuME; Kotani et al. 2005), at the Okayama Astrophysical Observatory (OAO) (Yanagisawa et al. 2010) on 67 nights; at the Akeno Observatory on 11 nights; and at the Ishigaki-jima Astronomical Observatory on 29 nights. Expanding the OISTER collaboration, we performed  $B$ ,  $V$ ,  $R$ , and  $I$ -band photometric observations on 29 nights using the 0.5-m (51-cm) telescope at Osaka Kyoiku University. The Kyoto Okayama Optical Low-dispersion Spectrograph (KOOLS; Yoshida 2005) attached to the Cassegrain focus of the 1.88-m OAO telescope

<sup>1</sup> We adopted  $t = 0$  as MJD 56132.39 derived by Chakradhari et al. (2014)

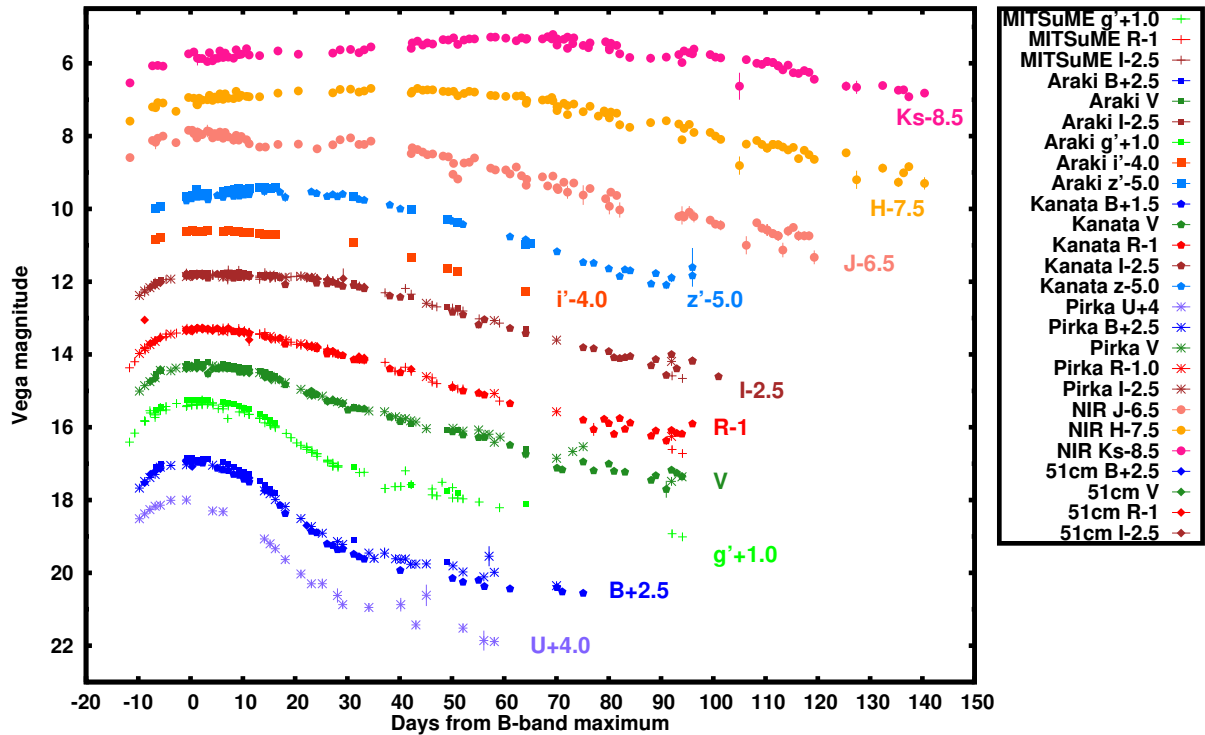


**Fig. 1.**  $U$ ,  $B$ ,  $g'$ ,  $V$ ,  $R$ ,  $I$ ,  $i'$ ,  $z' + Y$ ,  $J$ ,  $H$  and  $K_s$ -band light curves of SN 2012dn. The  $U$ ,  $B$ ,  $V$ ,  $R$  and  $I$ -band light curves are consistent with those presented in Chakradhari et al. (2014). Corrections have been made for Galactic and host galactic extinctions. The legend denotes the photometric data obtained by each instrument. The detailed observational modes are listed in Table 1.

was used for observations of the photometric standard stars on one night. These data were reduced using a standard procedure for charge-coupled device (CCD) photometry. The obtained data were reduced according to a standard procedure for ground-based observations. We performed point spread function (PSF) fitting photometry using the DAOPHOT package of the IRAF<sup>2</sup> reduction and analysis software.

## 2.2 Near-infrared photometry

$J$ ,  $H$ , and  $K_s$ -band photometric observations were performed over 80 nights using the Simultaneous three-color InfraRed Imager for Unbiased Survey (SIRIUS; Nagayama et al. 2003) installed on the 1.4-m InfraRed Survey Facility (IRSF) telescopes at the South Africa Astronomical Observatory (SAAO); the Nishi-harima Infrared Camera (NIC) installed at the Cassegrain focus of the 2.0-m Nayuta telescope at the Nishi-Harima Astronomical Observatory on 21 nights; and the InfraRed Camera installed on the 1.0-m telescope at the Iriki Observatory on 24 nights. The sky background was subtracted using a template sky image derived from each dithering observation set. PSF fitting photometry was conducted in a similar

manner to the optical.

## 2.3 Photometric calibrations

Photometric calibrations were performed using a similar method to Yamanaka et al. (2015). Relative photometry was carried out using the local reference stars in the field of SN 2012dn. For the NIR data, the 2MASS catalog magnitudes were used for the reference stars (Persson et al. 1998). A square average of the standard deviation of the SN and the systematic error of the reference star magnitudes were adopted for the observational errors. A summary of the results of the photometry is listed in Table 1 – 7. Photometric data for standard stars in the SA 111, SA 112, and SA 113 regions (Landolt 1992), which were obtained using HOWPol, MSI, Adler, and KOOLS on photometric observation nights, were used to calibrate the  $U$ ,  $B$ ,  $V$ ,  $R$ ,  $I$ ,  $g'$ ,  $i'$ , and  $z$ -band magnitudes of the reference stars. Using these magnitudes, relative photometry for the SN was performed. The calibrated reference magnitudes were consistent with those of Chakradhari et al. (2014), which lay within the error. Note that we reduced the systematic error for the various instruments using a color-term correction in a consistent manner and included newly performed observations of the standard stars in the M67 (Stetson 1987) and SA98 (Landolt 1992) regions.

<sup>2</sup> IRAF is distributed by the National Optical Astronomy Observatories, operated by the Association of Universities for Research in Astronomy, Inc., under contract to the National Science Foundation of the United States.



## 2.4 Optical spectroscopy

We performed optical spectroscopic monitoring using HOWPol over a period of 30 nights. The wavelength coverage was  $4,500 - 9,000 \text{ \AA}$  and the spectral resolution was  $R = \lambda/\Delta\lambda \sim 400$  at  $6,000 \text{ \AA}$ . During the data reduction procedure, the wavelengths were calibrated using telluric emission lines acquired in the object frames. The fluxes were calibrated using the frames of spectrophotometric standard stars taken on the same night as the object data. We removed strong telluric absorption features from the spectra using the spectra of high-temperature standard stars.

## 3 Observational properties

### 3.1 Light curves

Figure 1 shows the multi-band optical and NIR photometric data for SN 2012dn, where the magnitudes have already been corrected for Galactic and host galactic extinctions (Schlafly & Finkbeiner 2011; Chakradhari et al. 2014). *U*, *B*, *V*, *R*, and *I*-band data were consistent with those reported by Chakradhari et al. (2014), which lay within our error. The NIR light curves exhibited a single-peaked maximum, except for the *J*-band. Redder-band light curves arrived at their maximum at a later epoch. The *H* and *K<sub>s</sub>*-band maxima were particularly visible at  $\sim 40$  and  $\sim 70$  days after the *B*-band maximum date, respectively. Such large delays have never been found in any SNe Ia to date.

Figure 2 provides a comparison of the optical *U*, *B*, *V*, *R*, and *I*-band light curves with those of SNe 2001el (Krisciunas et al. 2004) and 2009dc (Yamanaka et al. 2009; Silverman et al. 2011; Taubenberger et al. 2011). The *U*-band data provide better coverage than those presented by Chakradhari et al. (2014). The rising part of the *U*-band light curve exhibited a slightly slower evolution than that of typical SN 2001el, while it was similar to that of another SC SN 2009dc (Taubenberger et al. 2011). The *U*-band maximum date was consistent with those of SNe 2001el and 2009dc. The rates of decline of the light curves for all bands were much slower than those of SN 2001el. The *B*-band light curve showed a significantly faster evolution than that of another SC SN 2009dc. The decline rates of the *U*, *V*, *R* and *I*-band light curves were relatively similar to those of SN 2009dc.

Figure 3 provides a comparison of the absolute magnitude light curves in the *J*, *H*, and *K<sub>s</sub>* bands of SN 2012dn with those of SNe 2001el and 2009dc. Additional data for SN 2009dc from Friedman et al. (2015) were included for this comparison. The light curves shown in Fig. 3 are the average of those of obtained within a night. The *J*-band light curve of SN 2012dn exhibited first and secondary maxima. The first peak was reached a few days after the *B*-band maximum, while for typical SN 2001el the first peak was reached a few days before the maximum. The

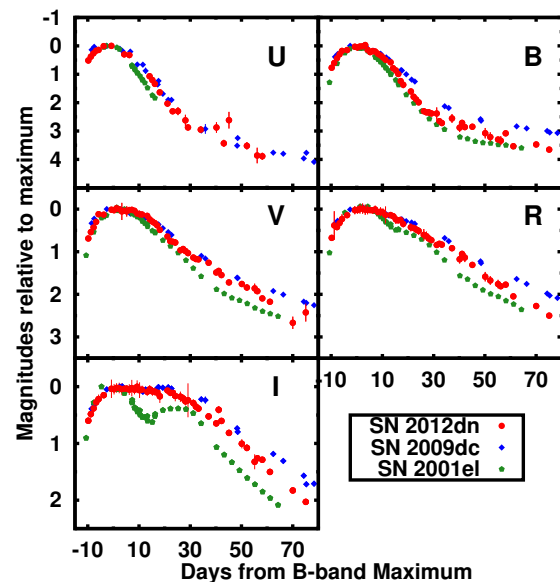


**Fig. 2.** *UBVRI*-band light curves of SN 2012dn compared to another well-observed SC SN 2009dc (Yamanaka et al. 2009; Silverman et al. 2011; Taubenberger et al. 2011) and a typical SN Ia 2001el (Krisciunas et al. 2004). Our data are denoted by the red-filled circles. Those of SNe 2001el and 2009dc are denoted by the blue diamond and green pentagons, respectively. The magnitudes were artificially shifted to their maximum for comparison. The data were stacked into the averaged magnitudes within a day from our data.

secondary peak occurred at  $t = 35$  d, which was similar to that of typical SN 2001el. The magnitude of the *J*-band secondary maximum was  $\sim 0.2$  mag fainter than the first, while that of SN 2001el was  $\sim 1.5$  mag fainter. The overall shape was fairly similar to that of SN 2009dc up to  $t = 40$  d, but the decline rate after  $t = 40$  d was much lower than that of both SNe.

For the *H* band, the magnitudes reached the maximum at around  $t = 40 - 50$  d. The light curve almost linearly declined from  $t = 40$  d until  $t = 140$ . The rate of decline was estimated to be 2.5 mag per 100 d between  $t = 40$  and 120 d, which was much slower than the 3.8 mag per 100 d between  $t = 20$  and 60 d for the typical SN 2001el. The shape of the light curve was comparable to that of SN 2009dc up to  $t = 20$  d, but the light curve was less luminous up to  $t = 40$  d. SN 2012dn had a much more luminous absolute magnitude than SN 2009dc after  $t = 45$  d, and the decline rate was much slower between  $t = 45$  and 110 d.

For the *K<sub>s</sub>* band, the above trend became even more noticeable. The light curve increased rapidly until  $t = 0$  d and then slowly evolved between  $t = 0$  and 40 d. The light curve reached its maximum at  $t = 60 - 70$  d. The decline rate was estimated to be 2.0 mag per 100 days between  $t = 70$  and 140 d, indicating that it had the slowest decline among the *U* to *K<sub>s</sub>* bands. The shape of the light curve of SN 2012dn was similar to that of SN 2009dc up to  $t = 25$  d. SN 2012dn became fainter than SN 2009dc after  $t = 40$  d, while its magnitude was 1.5 times more

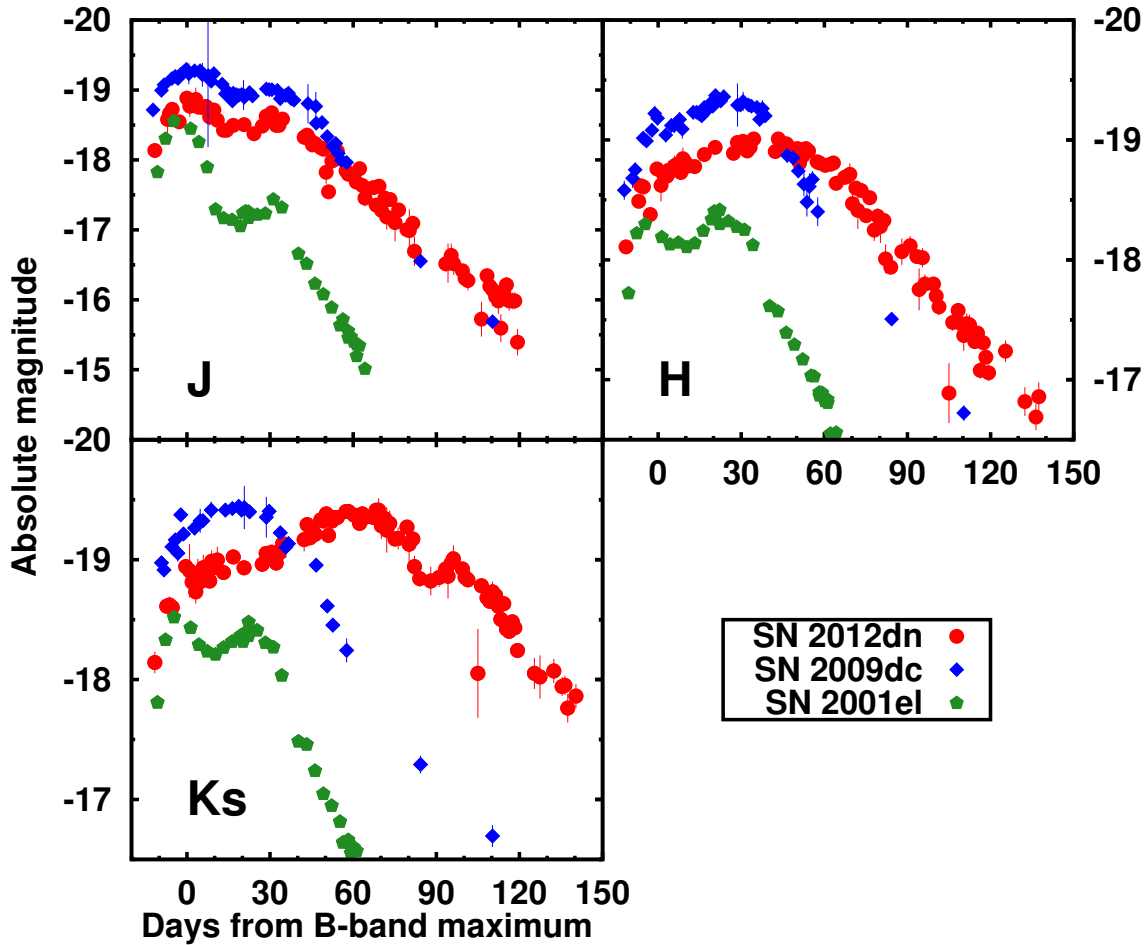


**Fig. 3.**  $JHK_s$ -band absolute magnitude light curves of SN 2012dn compared with those of SNe 2001el and 2009dc. Additional data for SN 2009dc from Friedman et al. (2015) were included for comparison. The absolute magnitudes of SN 2012dn were calculated using a distance modulus of  $\mu = 33.15$  to the host galaxy, ESO 462-16. SNe are denoted in a similar manner to Fig. 2. A dip at  $\sim 80 - 90$  days seen in  $H$  and  $K_s$  bands (and possibly in the  $J$  band) is probably a real feature, since the data independently obtained using different three telescopes were consistent within the systematic error. We stacked these data taken within a day into the averaged magnitudes. This feature would not contradict to the general interpretations for the NIR excess we examined in this paper, but this may contain information to further constrain on details of each scenario. We postpone such a study to the future.

luminous than SN 2009dc between  $t = 85$  and 110 d.

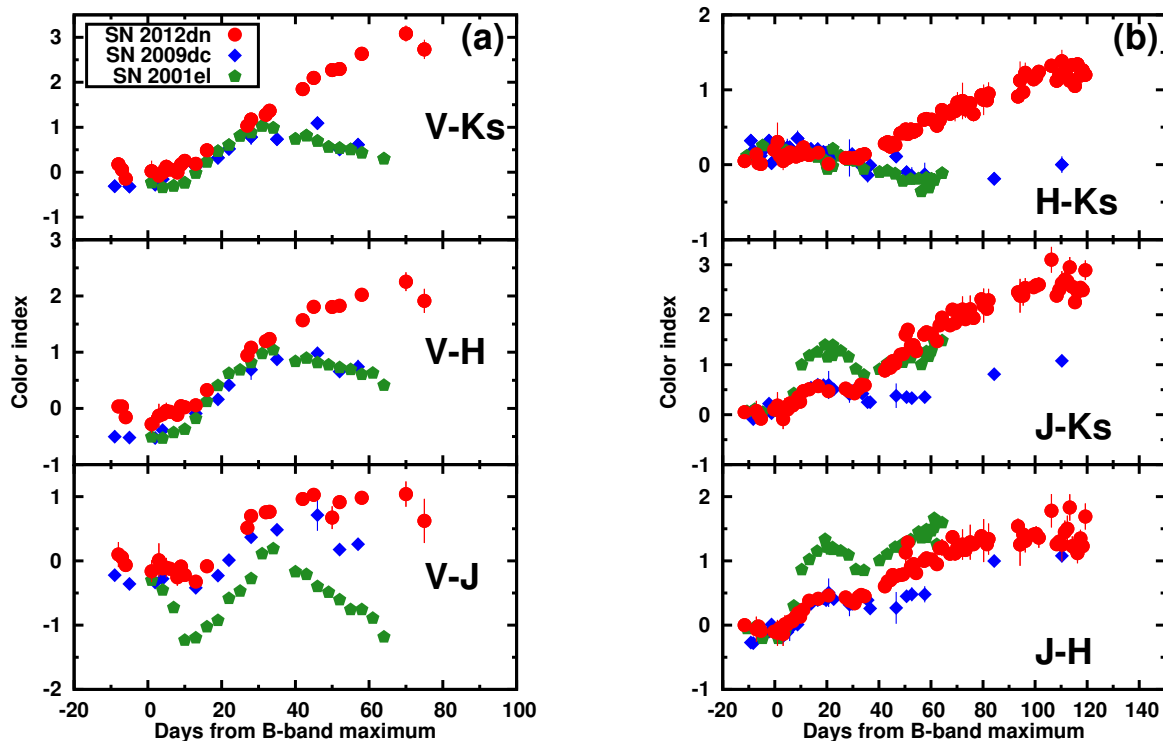
### 3.2 Color evolutions

Figure 4 provides a comparison of the  $V - J$ ,  $V - H$ , and  $V - K_s$  color evolutions with those of SNe 2001el and 2009dc. The  $V - J$  color exhibited a slow evolution to a much bluer color until  $t = 15$  d. Thereafter, the color evolved to become redder until  $t = 30$  d, becoming flat between  $t = 30$  and 100 d. The  $V - J$  color of SN 2012dn was always redder than that of SN 2001el, but was similar to that of SN 2009dc until  $t = 40$  d while reddening after  $t = 40$  d.

The  $V - H$  and  $V - K_s$  color evolutions are notable. The  $V - H$  color exhibited a monotonous evolution to a much redder color until  $t = 40$  d. Thereafter, the evolution slowed slightly

until  $t = 70$  d. The evolution up to  $t = 40$  d was similar to that of SNe 2001el and 2009dc, while the color became much redder than both SNe after  $t = 40$  d. Similar trends were confirmed for  $V - K_s$ , with the evolution up to  $t = 40$  d being similar to that of both SNe. The color was approximately  $\sim 3.0$  mag redder than that of both SNe at  $t = 60 - 70$  d.

Figure 4 also shows the  $J - H$ ,  $J - K_s$ , and  $H - K_s$  color evolutions compared with those of SNe 2001el and 2009dc. The color evolutions exhibited rather interesting behavior. The  $J - H$  color of SN 2012dn was always bluer than that of SN 2001el after  $t = 10$  d. The color began to evolve to be bluer up to  $t = 30$  d, similar to that of SN 2001el. The color evolution was also almost as fast as that of SN 2001el after  $t = 30$  d, while the color was bluer. In comparison with SN 2009dc, the color was similar to that until  $t = 35$  d, after which it became redder.



**Fig. 4.** (a)  $V - J$ ,  $V - H$ , and  $V - K_s$  color evolutions of SN 2012dn compared with those of SNe 2001el and 2009dc. The legends are the same as given in Fig. 2. (b)  $J - H$ ,  $J - K_s$ , and  $H - K_s$  color evolutions compared with those of SNe 2001el and 2009dc. Symbols are denoted in the same manner as in Fig. 2.

Similar trends were observed in the  $J - K_s$  color evolution. The break points at  $t = 30$  d came slightly earlier than those of SN 2001el, and the evolution slope was marginally bigger after the  $t = 30$  d period. The color became redder than that of SN 2001el after  $t = 50$  d, but the color evolution was similar to that of SN 2009dc up to  $t = 30$  d, becoming much redder than that of SN 2009dc at  $t = 35$  d.

The  $H - K_s$  color evolution was similar to that of SNe 2001el and 2009dc until  $t = 30$  d. Thereafter, the color evolved to become redder while those of SNe 2001el and 2009dc became bluer. The deviation of the  $H - K_s$  color evolution of SN 2012dn implies that there is an external component in the NIR region. The subtraction of the NIR light curves by those of SN 2009dc is carried out in §5.1 to clarify the nature of this external component.

### 3.3 Bolometric luminosity

The  $BVRI$  and  $BVRIJHK_s$  -band integration light curves were constructed using the full width half maximum (FWHM) and the center wavelengths of their passband (Fukugita et al. 1996). Galactic and host galactic extinctions were corrected using  $E(B - V) = 0.1$  (Chakradhari et al. 2014). A distance modu-

lus of  $\mu = 33.15$  was adopted (Theureau et al. 1998). Additional data from Chakradhari et al. (2014) were also included. The optical-NIR integration light curve was compared with the optical alone to assess whether the NIR excess originated from a different component from the SN emission. For comparison, the  $BVRIJHK_s$  and  $BVRI$  -band integration light curves of another SC SN 2009dc and the template SN Ia were also constructed (Hsiao et al. 2007) (see Fig. 5). The absolute magnitudes of the template were obtained from the decline rate for a normal SN Ia ( $\Delta m_{15}(B) = 1.1$ ; Phillips et al. 1999)

The peak luminosity was estimated to be  $7.0 \times 10^{42}$  erg  $s^{-1}$ . Assuming that the luminosity was 60% in the  $BVRIJHK_s$  -band coverage region (Stritzinger et al. 2006), the quasi-bolometric luminosity was calculated to be  $1.2 \times 10^{43}$  erg  $s^{-1}$ . The luminosity was 25% fainter than the luminosity estimated using a similar method by Chakradhari et al. (2014). This difference could be caused by a systematic error. The peak luminosity was slightly fainter than that of the template light curve, indicating that the absolute luminosity of SN 2012dn was similar to normal SNe Ia. The peak luminosity was 2.3 times fainter than that of the extremely luminous SN 2009dc.

There was a slight difference in the decline of the light curve between the optical and optical-NIR integrations. The de-

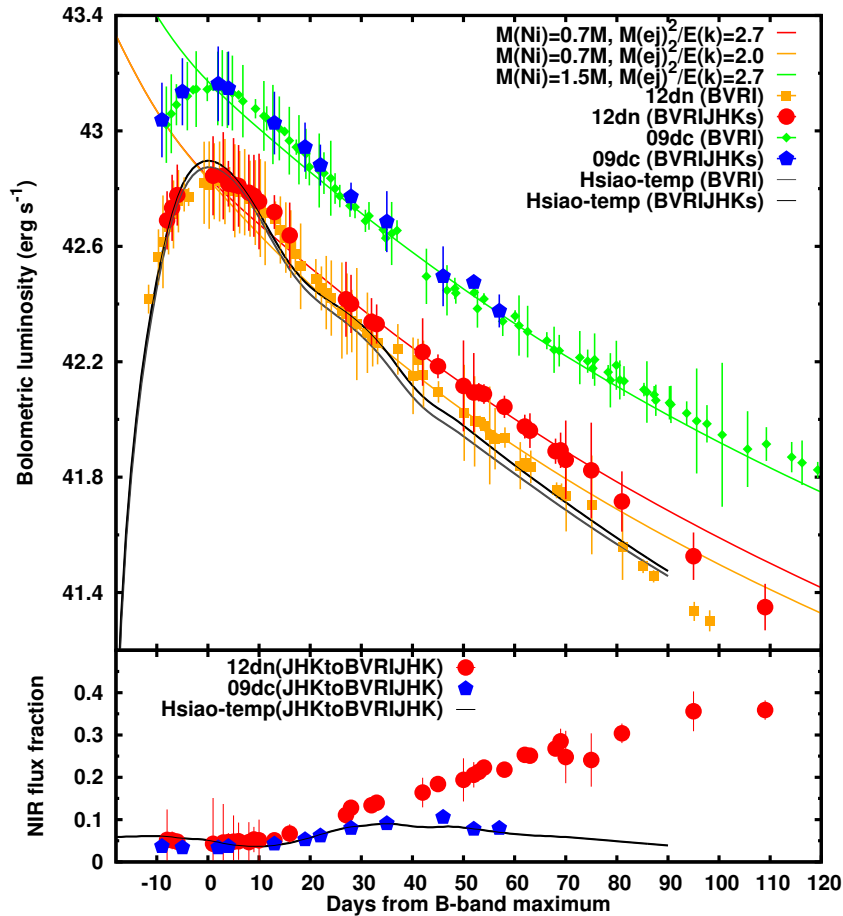


**Fig. 5.** (Top panel) Quasi-bolometric light curves of SN 2012dn integrated with *BVRI* and *BVRIJHK<sub>s</sub>*-band photometric data, which are denoted by the orange-filled squares and red-filled circles, respectively. The light curves of SC SN 2009dc (Yamanaka et al. 2009; Silverman et al. 2011; Taubenberger et al. 2011) and the SN Ia template (Hsiao et al. 2007) are plotted for comparison. The analytical light curves with  $(M/M_{\odot}) \cdot (E_K/10^{51} \text{ erg s}^{-1})^{-1} = 2.0$  and 2.7 are also plotted. The  $^{56}\text{Ni}$  mass was  $0.7M_{\odot}$  for both analytical curves. They are denoted by the orange and red lines, respectively. The analytical light curve for SN 2009dc with  $(M/M_{\odot}) \cdot (E_K/10^{51} \text{ erg s}^{-1})^{-1} = 2.7$  is also plotted. (Bottom panel) Flux fraction evolutions of the *JHK<sub>s</sub>* to *BVRIJHK<sub>s</sub>*-band integration flux of SNe 2012dn and 2009dc. That of the SN Ia template is also plotted and is denoted by the black line. Symbols are the same as for the upper panel.

cline rate of the *BVRIJHK<sub>s</sub>*-band light curve between  $t = 0$  and 75 d was estimated to be  $8.5 \times 10^{40} \text{ erg s}^{-1} \text{ d}^{-1}$ , which was marginally slower than the  $8.7 \times 10^{40} \text{ erg s}^{-1} \text{ d}^{-1}$  for the *BVRI*-band integration. The difference increased at later epochs. The decline rates of the *BVRIJHK<sub>s</sub>* and *BVRI*-band integration light curves of SN 2009dc were comparable.

The both light curves exhibited the faster decline than the analytical models after  $t = 80$  d. Later-epoch light curve for another SC SN 2006gz also exhibited faster decline (Maeda & Iwamoto 2009; Chakradhari et al. 2014). Those of SNe 2007if and 2009dc were quite slower (Chakradhari et al. 2014). There could be diversity of the light curve decline among SC SNe. Thus, the faster decline of the light curve of SN 2012dn could be intrinsic. On the other hand, the NIR light curves exhibited slower evolution after  $t = 80$  d, indicating the echo component (see §5.2.2), but the energy contributions were relatively small.

The evolution of the NIR contribution was then investigated. The lower panel of Fig. 5 shows the time evolution of the NIR flux fraction in the optical-NIR integration light curve. The NIR flux dramatically increased after  $t = 15$  d. This was earlier than our expectation based on a comparison of the color evolutions with those of SNe 2001el and 2009dc (see §3.2). The NIR flux contribution became 35 % of the total optical-NIR integration flux at  $t = 110$  d. On the other hand, the NIR contributions of normal SNe Ia and 2009dc were lower than those at earlier epochs (Sollerman et al. 2004; Wang et al. 2009). This was a unique feature of SN 2012dn.

<sup>3</sup> <http://bruford.nhn.ou.edu/suspect/index.html>

<sup>4</sup> <http://wiserep.weizmann.ac.il/>



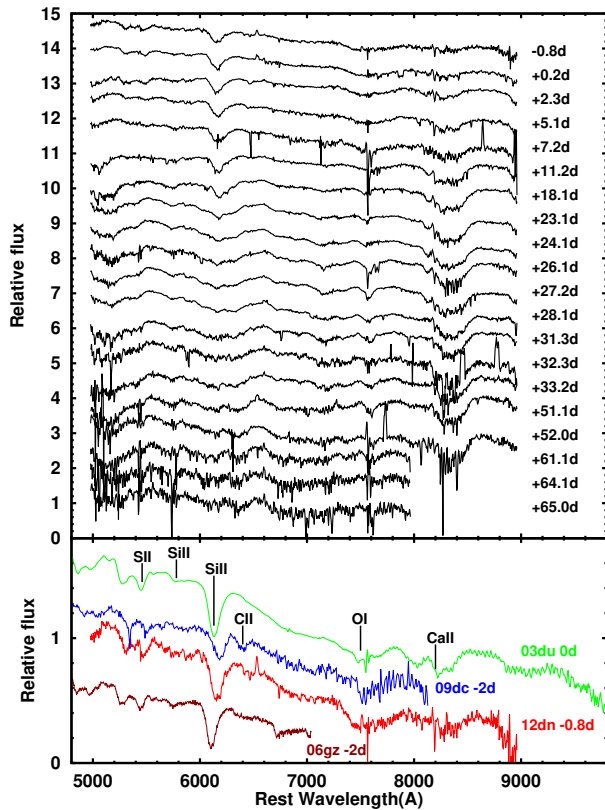


**Fig. 6.** (Top panel) Time series of the spectra of SN 2012dn obtained by HOWPol between  $t = -0.8$  and  $65.0$  d. The wavelengths were converted to the rest frame using the recession velocity of the host galaxy, ESO 462-16. The atmospheric absorption lines were corrected using the spectra of standard stars obtained on the same night as the objects. (Bottom panel) The spectrum at the maximum compared to those of SNe 2003du (Stanishev et al. 2007), 2006gz (Hicken et al. 2007) and 2009dc (Yamanaka et al. 2009). The data for SNe 2003du and 2006gz were taken from the SUSPECT database<sup>3</sup>.

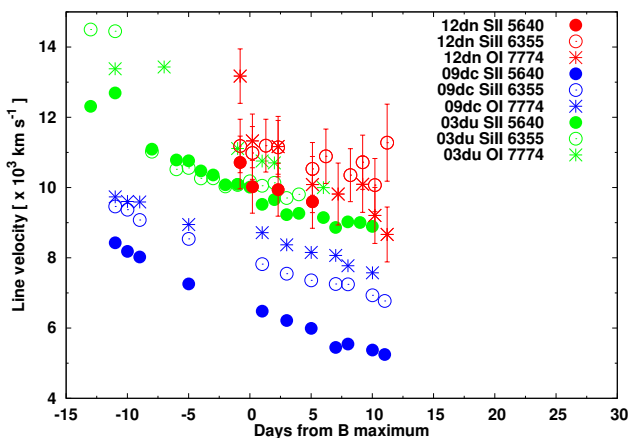


**Fig. 7.** Line velocity evolutions of the O I  $\lambda 7774$ , Si II  $\lambda 6355$ , and S II  $\lambda 5640$  absorption lines of SNe 2009dc and 2012dn. The data for SNe 2003du and 2009dc were taken from the SUSPECT and WISEREP<sup>4</sup> databases. Measurements of the absorption lines were performed using the *splot* command in IRAF. The error was calculated by summing the standard deviations and wavelength resolution.

### 3.4 Spectral properties

The spectral evolution of SN 2012dn is shown in Fig. 6. The wavelengths of the data were corrected using the recession velocity of the host galaxy (Theureau et al. 1998). The spectra exhibited the multiplet of the Fe II, Si II, S II W-shape features, the Ca II IR triplet, and the O I, indicating that this SN should be classified into the subclass of SNe Ia (Branch et al. 1993). The strong C II  $\lambda 6580$  and  $\lambda 7234$  absorption lines were detected until  $t = 25$  d, which was 10 days later than the last one reported by Chakradhari et al. (2014), although these may be contaminated by Fe II absorption during the later phase because emission lines from iron-group elements are dominant in the inner-ejecta region. The C II absorption lines after the *B*-band maximum are also confirmed in SN 2009dc (Yamanaka et al. 2009).

We measured the absorption minima, O I  $\lambda 7774$ , Si II  $\lambda 6355$ , and S II  $\lambda 5640$ . The line velocities of these features of the normal SN 2003du (Stanishev et al. 2007) and SC SN 2009dc were also measured in the same manner. The measured features were identified as indicated in the lower panel of Fig. 6 by comparison with those of well-studied SC SNe (Hicken et al. 2007; Yamanaka et al. 2009). The line velocity evolutions are also shown in Fig. 7. The decline rate of the line velocity evolution of S II was the largest among these features. Similar trends were also detected in SNe 2003du and 2009dc. The Si II line velocity exhibited a moderate decline, which was similar to those of SNe 2003du and 2009dc. In contrast to the decline rates of Si II and S II, the decline rate of the O I line velocity was much larger than that of SN 2009dc. Finally, the velocities of all the elements were 1.3 – 1.7 times faster than those of SN 2009dc, but similar to those of SN 2003du near the *B*-band maximum.

## 4 Classification as a super-Chandrasekhar SN Ia

Chakradhari et al. (2014) reported that the spectral properties displayed a resemblance to those of the SC SN candidate SN 2006gz. The strong C II and shallow Si II absorption lines were similar to those of other SC SNe, and the line velocities were comparable to those of SN 2006gz, rather than the SNe 2003fg and 2009dc. They concluded that SN 2012dn could be classified as a SC SN. Here, we support their results by focusing on the NIR observational properties.

The light curves a normal SN Ia exhibited, the characteristic structures around  $t = 20 - 30$  d, e.g., the shoulder-like structure of the *R*-band. For normal SNe Ia, the secondary maximum magnitudes of the *I* and *J*-band light curves were much fainter than the first peak. On the other hand, SNe 2012dn and 2009dc exhibited much flatter shapes in all bands than those of normal SN 2001el. Moreover, the shapes of the light curves of SNe 2012dn and 2009dc up to  $t = 40$  d were extremely similar.

Similar trends were also exhibited by the color evolutions. The  $V - J$ ,  $J - H$  and  $J - K_s$  color evolutions demonstrated an excellent match with those of SC SN 2009dc, while remaining quite distinct from those of normal SNe Ia. Contrastingly,  $V - H$  and  $V - K_s$  color evolutions were well similar to those of SNe 2001el and 2009dc, while the  $V$ ,  $H$ , and  $K_s$ -band light curves were quite different. The NIR light curves and color evolutions among the SNe Ia exhibited greater homogeneous characteristics than those of the optical (Jack et al. 2012; Dhawan et al. 2015).

The estimated ejecta mass ranged from  $\sim 1.8 - 2.2 M_\odot$  using various approaches (see Appendix 1), indicating that the total ejected mass could be much larger than the Chandrasekhar-limiting mass of a non-rotating WD (but, see Parrent et al. 2016). Such a mass range for SN 2012dn is roughly consistent with those derived from the light curve and spectral analysis of SC SNe (Scalzo et al. 2010; Silverman et al. 2011; Taubenberger et al. 2011; Kamiya et al. 2012; Hachinger et al. 2012). We conclude that SN 2012dn should be classified as a SC SNe.

## 5 Discussion

### 5.1 NIR excess

SN 2012dn shows an additional and extremely long-duration component in the NIR light curves. In the following sections, we extract this NIR component using light curve subtraction, and analyze the spectral energy distribution using dust models.

#### 5.1.1 NIR light curve subtraction

The subtraction of the  $J$ ,  $H$  and  $K_s$ -band fluxes by those of another SC SN 2009dc, was performed to derive the origin of the NIR excess. The  $J$ ,  $H$ , and  $K_s$ -band light-curve shapes exhibited the excellent matches to those of SN 2009dc up to  $t = 40$  d, indicating that the intrinsic NIR light-curve behavior is almost the same to that of SN 2009dc while the absolute luminosities were different. From this striking similarity, we hereafter assume that the behavior intrinsic to the SN components are the same between SNe 2012dn and 2009dc, and we discuss the origin of the difference between two SNe. While we believe this is a reasonable assumption, further justification of this assumption will require a larger sample of NIR light curves of SC SNe Ia, highlighting the importance of intensive NIR follow-up observations of SC SNe Ia.

First, the  $J$ ,  $H$ , and  $K_s$ -band absolute magnitudes of SNe 2009dc and 2012dn were measured at their  $B$ -band maximum. The fluxes were converted from these magnitudes using the FWHMs of the filter passbands and zero magnitude fluxes (Fukugita et al. 1996; Bessell 1990). The fluxes of SN 2012dn were subtracted by those of SN 2009dc. Stretching of the light curves was not performed because the  $JHK_s$ -band light curves

of SN 2012dn were similar to those of SN 2009dc up to  $t = 30$  d (see §4). When the fluxes of SN 2009dc were absent during the same epoch as those of SN 2012dn, the interpolation was performed for the fluxes of SN 2009dc. The subtracted fluxes were converted into absolute magnitudes and are plotted in Fig. 8.

The subtracted  $H$  and  $K_s$ -band light curves exhibited linear rises until  $t = 40$  and  $50$  d, respectively, and the  $H$  and  $K_s$ -band peak magnitudes reached  $-18$  and  $-18.5$  mag, respectively. Thereafter, they exhibited notable plateaus in the  $H$  and  $K_s$  bands. The subtracted  $J$ -band component began to be visible at a magnitude of  $-15.5$  after  $t = 90$  d, after the SN emission became sufficiently faint. Such plateau-shaped light curves could naturally be explained by the NIR echo from the CS dust (Maeda et al. 2015). Comparisons of the subtracted light curves with the theoretical model will be performed in §5.2.2.

#### 5.1.2 Dust model fitting

The SEDs of the subtracted  $H$  and  $K_s$ -band fluxes were constructed from the effective wavelengths of the passband of their filters (Bessell 1990; Fukugita et al. 1996). Fitting to the subtracted SEDs using the dust model from Kawabata et al. (2000) was then performed adopting the following procedure. The dust emission SEDs were calculated using the Mie theory for dust opacities. The optically thin dust emissions were integrated on the assumption of a distribution of the dust sizes; the power-law index was assumed to be 3.5. We calculated two cases of the dust composition: amorphous carbon and astronomical silicate (Kawabata et al. 2000). The dust temperatures and masses were given as variable free parameters. The temperatures were varied at every 100 K in the range between 500 and 2500 K, and the dust masses varied from  $10^{-6}$  to  $10^{-4} M_\odot$ . To derive the most reliable parameters, a least-squares method was adopted. The SED and dust model evolutions are shown in Fig. 9. We found that SED fitting after  $t = 45$  d was more reliable.

The temperature evolution was derived from the SED fitting analysis. Figure 10 shows that the dust temperature evolution exhibited an exponential decrease between  $t = 40$  and 100 d. In particular, it seems to exhibit a flat evolution after  $t = 60$  d. Figure 10 also shows that the dust mass evolution displayed an increase from  $10^{-6}$  to  $10^{-4} M_\odot$ . It appears to show a flat evolution from  $t = 60$  d, although this is later than the beginning of the  $K_s$ -band plateau phase. Fitting to the  $J$ ,  $H$ ,  $K_s$ -band fluxes was also performed between  $t = 90$  and 110 d. These results may be more reliable than just the  $H$  and  $K_s$ -bands because the SN component was much fainter than the dust emission at this point. We will discuss this in the following section, assuming that the fitting result is significant only after  $t = 45$  d.

Until now, amorphous carbon was used in the analysis of the SED fits. We also attempted SED fitting at similar epochs using the astronomical silicate model (Kawabata et al. 2000). Figure

9 shows a comparison of the dust emission SED of amorphous carbon with that of astronomical silicate at  $t = 70$  d. The temperatures used to explain the SEDs among these phases ranged from 1200–2200 K and were significantly higher than the evaporation temperature of astronomical silicate,  $\sim 1000$  K (Nozawa et al. 2003). This means that the dust that accounts for the NIR excess of SN 2012dn could almost completely be dominated by amorphous carbon. We will discuss the origin of this dust in the following section, and adopt amorphous carbon with a grain size of  $0.01\mu\text{m}$ .

## 5.2 Origin of the dust

The near-infrared excess related to the dust has previously been discussed for several core collapse SNe (Bode & Evans 1980; Dwek et al. 1983; Dwek 1983; Gerardy et al. 2000; Pozzo et al. 2004; Mattila et al. 2008; Di Carlo et al. 2008; Fox et al. 2009; Andrews et al. 2011; Maeda et al. 2013; Gall et al. 2014). However, there have been only a few discussions regarding dust signatures for the subclass of SNe Ia, i.e., SN 2005gj-like events (Fox et al. 2013). SN Iax 2014dt also exhibited a possible mid-infrared (MIR) excess in the intermediate phase, suggesting that dust emission could arise from an NIR echo or other mechanisms (Fox et al. 2016). They also presented a  $K_s$ -band light curve which might show a glowing excess, while they did not discuss the origin of the possible  $K_s$ -band excess. The scenarios that could explain the NIR excesses include (i) ejecta cooling condensations, (ii) light echo from the interstellar/circumstellar medium, and (iii) dust formation through the interaction of the ejecta with the CSM. For SN 2012dn, no emission lines were found in its early spectrum, indicating that the ejecta-CSM interaction scenario is unlikely.

### 5.2.1 Dust formation

The NIR echo scenario could be naturally acceptable by the fact that the NIR light curves subtracted by those of SN 2009dc exhibited definitively trapezoidal shapes (see §5.2.2). The dust formation scenario does not explain the serendipitous reproduction of such plateau evolutions. Most SNe that undergo dust formation exhibit a significant increase in the NIR fluxes, e.g., as observed in SN IIn 2005ip (Fox et al. 2009). The blueshift of the emission lines, the sudden drop in the optical luminosity, a slight increase in the NIR emission, the reddening of the optical color, and the evolutions of the optical depth were not found in observations of SN 2012dn. To clarify these points, we discuss in this section whether the dust formation scenario can explain the NIR excess observed in SN 2012dn or not.

Recently, it has been reported that SC SNe have a relatively fast decline in their optical light curves between  $t = 200$  and 400 d (Maeda et al. 2009; Taubenberger et al. 2011). Analysis suggests that this fast decline may be related to dust formation

scenario. For SN 2012dn, Chakradhari et al. (2014) reported that the optical light curves exhibited a faster evolution between  $t = 50$  and 100 d compared with those of other SC SNe 2007if and 2009dc, but were similar to those of SN 2006gz. The authors suggested that dust condensation may occur from  $t = 50$  d, which was much earlier than that discussed for other SC SNe.

Indeed, the optical-NIR integration light curve exhibited a similar decline rate to that of SN 2009dc (see §3.3). Such serendipitous consistency may be explained by re-emission from the newly formed dust absorbing the SN emission. However, it is not clear whether the consistent evolution of the SN light curves are intrinsic or not.

From a theoretical point of view, Nozawa et al. (2011) predicted that dust formation should occur at a much later epoch, i.e., a year after the explosion. Furthermore, a higher-density ejecta relative to a normal SN Ia could further delay dust formation. Therefore, the timescale of the NIR increase seems to be too short to be consistent with the dust formation scenario.

If typical-sized dust forms via ejecta cooling, the bluer band color should experience more substantial extinction. In our case, the  $U - B$  color did not exhibit significant reddening between  $t = 30$  and 60 d (Chakradhari et al. 2014), and the evolution was similar to that of SN 2009dc. On the other hand, the  $B - V$  color was  $\sim 0.4$  mag redder than that of SN 2009dc between  $t = 30$  and 60 d. Other optical colors were similar to those of SN 2009dc (Chakradhari et al. 2014). Therefore, if the dust formation would be responsible to the fast decline in the optical light curve, anomalous dust with wavelength independent opacity is needed to explain these similar color evolutions, e.g., a gray dust.

SED fitting analysis either does not favor the dust formation scenario. The optical depth evolution could show a rapid increase if dust formation occurs in the ejecta, as observed in Type Ibn SN 2006jc (Di Carlo et al. 2008; Mattila et al. 2008; Sakon et al. 2009). The optical depth did not exhibit the dramatical evolution among  $t = 40$  and 70 d, suggesting that mass evolution by the newly formed dust was unconfirmed. The dust mass evolution also exhibited a flat evolution until  $t = 100$  d, implying that no new dust formation occurred between  $t = 40$  and 100 d (see Figure 10). All these arguments presented in this subsection support the NIR echo scenario rather than the dust formation.

### 5.2.2 Light echo from circumstellar dust grains

The subtracted  $H$  and  $K_s$ -band light curves exhibited flat evolutions between  $t = 50$  and 110 d. A NIR echo could be the most plausible scenario to explain such flat evolutions (Dwek 1983; Chevalier 1986). A comparison of the subtracted light curves with those predicted by the theoretical model (Maeda et al. 2015) was performed in two cases. Estimating the distances to the CS dust using the epoch of the beginning of the

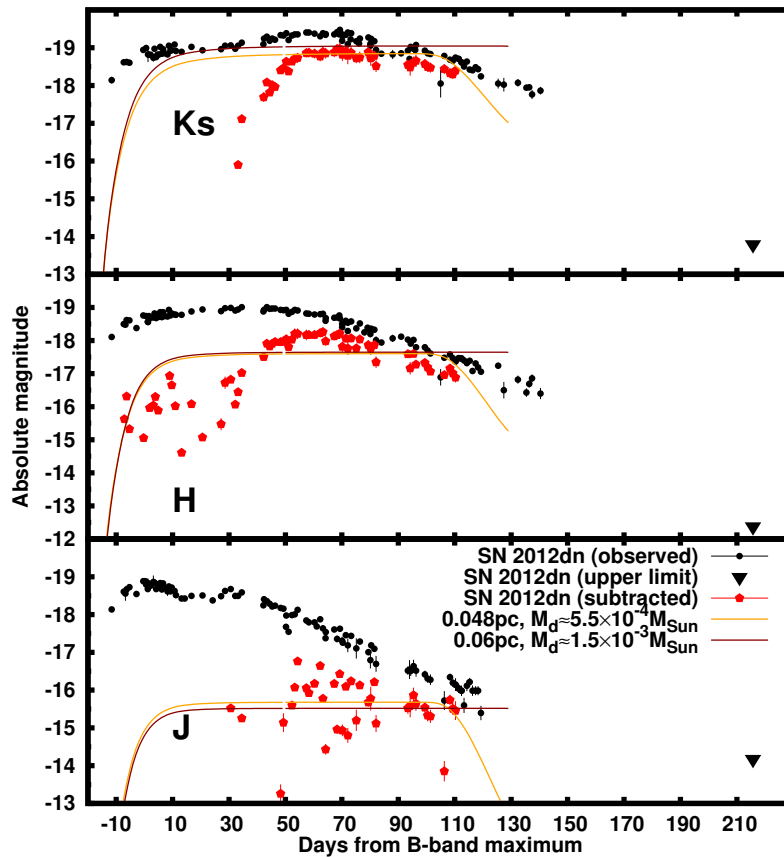


**Fig. 8.** Comparison of the absolute magnitude light curves of SN 2012dn with the theoretical NIR echo models (Maeda et al. 2015) using two different sets of the parameters, and assuming a symmetrically spherical shell and amorphous carbon. The light curves subtracted by those of SN 2009dc are also plotted and are denoted by the red-filled pentagon. The upper-limit magnitudes observed by IRSF telescope were also plotted and denoted by the down triangles.

NIR echo and the duration of the plateau, we investigated the distance over which the dust can survive in the SN radiation field.

The duration of a light curve is determined by the spatial extent of the interstellar/circumstellar dust. Dust emission that is thermalized by the radiation of the central SN is seen by an observer. For a sample of normal SNe Ia, Maeda et al. (2015) provided upper limits for the CS dust masses and their distances from SNe by comparing the predicted NIR echo light curves with observations. We attempted to compare the  $JHK_s$ -band light curves of SN 2012dn with the theoretical light curves as shown in Fig. 8. To explain the subtracted  $J$ ,  $H$  and  $K_s$ -band luminosity, the dust mass should be  $5.5 \times 10^{-4} - 1.5 \times 10^{-5} M_{\odot}$ , with the dust assumed to have a shell-like geometry and consist of amorphous carbon. The distances to the dust in the model were assumed to be  $\sim 4.8 \times 10^{-2} - 6.0 \times 10^{-2}$  pc. It should be emphasized that this model can simultaneously explain all NIR-band luminosity with consistent masses, indicating the consistency in the dust temperature between the model and in SN 2012dn. However, it does not explain the rising part of the subtracted light curves.

A spherically symmetric shell cannot explain the time delay at the beginning of the NIR echo. The dust would not be distributed around the crosspoint between the line-of-sight direction and the circular. The smallest distance was calculated to be  $\sim 2.0 \times 10^{-2}$  pc if the dust was located on the opposite side of the SN to the Earth, although such geometry is highly unlikely. The longest distance is limited by the intensity of the SN radiation and the temperature of the dust (this will be discussed in the following paragraph). Thus, we suggest that a reasonable distance could be greater than  $2.0 \times 10^{-2}$  pc, which is not inconsistent with the distances estimated from the theoretical model. An axisymmetrically circular arc shell could explain such a delay. Alternatively, a highly inclined ring-like shell could also be considered. Future work on the NIR echo emission for a SC SN Ia will deal with such problems. The nature of the pre-explosion system is discussed, using these distances and CS dust shell geometries, in §5.3.

The minimum dust cavity size can also be limited using the peak luminosity because the strong radiation field can break up the dust particles (Dwek 1983). The scaling method for the parameters of the well-studied SN to those of SN 2012dn is



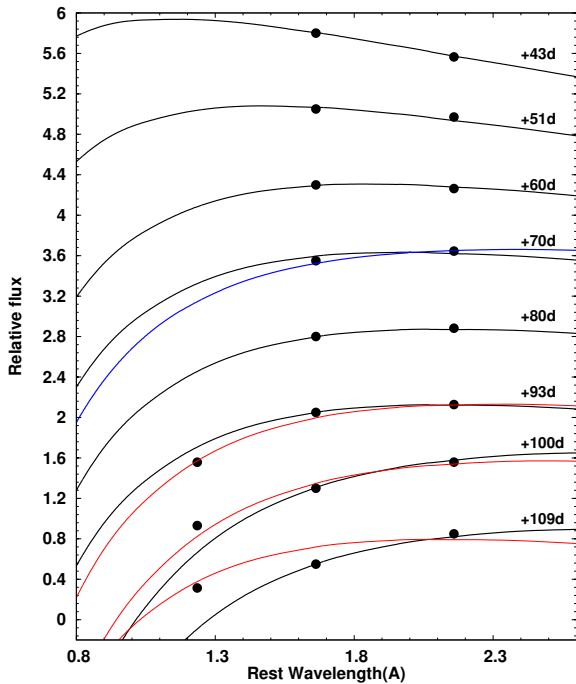


**Fig. 9.** Time evolution of the spectral energy distributions (SEDs) of SN 2012dn between  $t = 43$  and 109 d. The SEDs were converted from the light curves subtracted by those of SN 2009dc. Each epoch is denoted at the top right side of each SED. Each line denotes a dust emission model (Kawabata et al. 2000). The dust emissions were calculated by integrating the optically thin dust using an assumed power-law size distribution. The maximum size was  $0.01\mu\text{m}$ . The dust was composed of amorphous carbon. The blue line denotes a model for astronomical silicate whose temperature significantly exceeds its evaporation temperature. The black lines denote the fitting results for the  $H$  and  $K_s$ -band fluxes, while the red line denotes the  $J$ ,  $H$ , and  $K_s$ -bands.

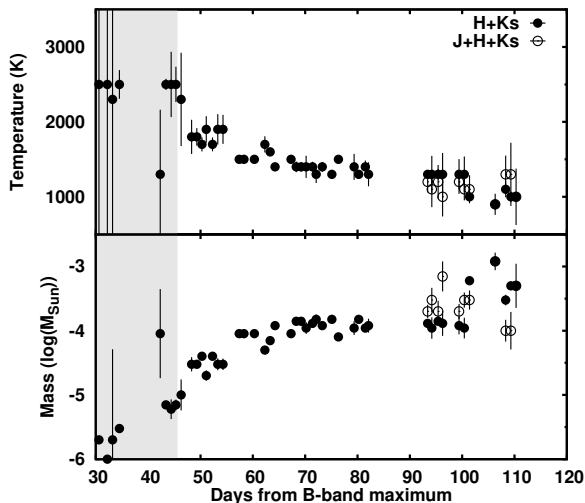


**Fig. 10.** (Top panel) Time evolution of the dust temperatures estimated from the SED fitting analysis. The parameters used for the dust emission models are the same as those presented in Fig. 9. The estimated values in the shaded regions are unreliable. (Bottom panel) The dust mass evolutions estimated by the same method as the upper panel.

used along with Eq. (5) presented in Fox et al. (2009). SED fitting estimated the dust temperature to be  $T_d \sim 1300$  K at the plateau phase. The peak luminosity was already estimated to be  $L = 1.2 \times 10^{43}$  erg  $\text{s}^{-1}$  from the  $BVR IJHK_s$ -band integration light curves (see §3.3). We used the following parameters for the scaling method: a dust cavity size of  $r = 6.0 \times 10^{16}$  cm, temperature of  $T_d = 1900$  K, and  $L_{peak} = 1.4 \times 10^{43}$  erg  $\text{s}^{-1}$  for Type II SN 1980K as a template (Dwek 1983). The size of the dust cavity was estimated to be  $\sim 1.4 \times 10^{17}$  cm, which corresponds to  $4.6 \times 10^{-2}$  pc. This is consistent with the size estimated from the theoretical NIR echo model.

We have presented an illustration of the NIR echo scenario by comparing the subtracted light curves with those predicted by the theoretical model. The distance ( $\sim 4.8 - 6.0 \times 10^{-2}$  pc) estimated from the theoretical model was consistent with the lower limit ( $\sim 4.6 \times 10^{-2}$  pc) set by the condition of the dust evaporation. Indeed, this is in support of the NIR echo scenario where the most significant contribution to the NIR LC comes from the dust at the evaporation radius, even if the CSM is distributed smoothly from the SN vicinity.

### 5.3 Implications for the progenitor system

A non-rotating WD explosion in the single-degenerate scenario cannot reproduce the super-Chandrasekhar-limiting mass. There are two possibilities to account for the large ejecta mass: a rapidly-rotating WD or a double WD merger scenario. In a recent hydrodynamic explosion model, the extremely large luminosity (i.e., the large  $^{56}\text{Ni}$  mass) favors the detonation-triggered spherical explosion of a rapidly rotating WD in the single-degenerate scenario (Pfannes et al. 2010), while a violent merger-induced explosion from the double-degenerate scenario would explain the subluminous (Pakmor et al. 2010) or normal SNe Ia (Pakmor et al. 2012).

A recurrent nova is an explosive event caused by thermonuclear runaway on the surface of the WD by accretion from a companion star, e.g., a red giant star. If the mass accretion from the companion is superior to the mass loss by the eruption, the WD mass grew up to the limiting mass. Thereafter, the thermonuclear explosion of the entire WD material should occur (Hachisu et al. 1999; Hachisu et al. 2012). The Roche lobe overflow caused by the binary interaction also leads to a dense environment surrounding the system. The single-degenerate scenario favors such a dense environment around the progenitor.

The envelope predicted by the merger scenario would be expected to be ejected within  $\sim 1$  day after the disruption of the secondary star (Yoon et al. 2007; Levanon et al. 2015; Tanikawa et al. 2015). The interaction of the ejecta with such a close envelope may rather predict the UV excess at the earlier phase (Scalzo et al. 2010; Scalzo et al. 2012; Brown et al. 2014; Brown 2014). The density on the subparsec scale is low because the



time scale over which the merger event of the two WDs occurs is very long due to the formation of the WD binary.

Our analysis found that the NIR echo light curve of SN 2012dn between  $t = 40$  and 110 d is well explained by the existence of CS material surrounding the pre-explosion system in the single-degenerate scenario. Such an NIR echo implies that the pre-explosion material existed at a distance greater than  $\sim 4.6 \times 10^{-2}$  pc. Such distant material strongly supports the presence of a wind from the pre-explosion system, e.g., a recurrent nova.

The mass loss rate of the pre-explosion system can be estimated within the framework of the NIR echo scenario. The radius and the total mass of the CS dust are required. The former was calculated using the timescale over which the NIR echo luminosity sufficiently decreased, and was adopted to be  $R = 1.8 \times 10^{17}$  cm. The total mass was adopted as  $M_d \sim 5.5 \times 10^{-4} - 1.5 \times 10^{-3} M_\odot$  from the comparison with the theoretical NIR echo. Given that the model overpredicts the early rising light curve, the mass should be reduced by a factor  $\sim 2$ . The gas-dust mass ratio was assumed to be  $Z_d = 0.01$ . The mass loss rate was calculated to be  $4.8 \times 10^{-6} - 1.3 \times 10^{-6} M_\odot \text{ yr}^{-1}$ , assuming that the shell velocity was  $10 \text{ km s}^{-1}$ . The estimated mass loss rate ( $\sim 10^{-6} - 10^{-5} M_\odot \text{ yr}^{-1}$ ) is roughly consistent with those measured from Galactic recurrent novae (Hachisu et al. 2000; Hachisu & Kato 2001).

The deep images of Galactic SN Ia progenitor candidates V445 pup and RS Oph obtained several years after their eruptions have been reported (Woudt et al. 2009; Bode et al. 2007). Axisymmetric bipolar shells formed by the ionized gases were found, and these exhibited a mildly spread opening angle. The time delay and durations of the NIR echo in SN 2012dn are likely to be explained by such geometry even if the line-of-sight direction is parallel to the CS shell plane. Another NIR echo from the opposite side of the shell surrounding SN 2012dn would reach us in the near future, depending on the geometry. Alternatively, the interaction of emission from the collision of the ejecta with the shell may be discovered. Assuming that the ejecta velocity is  $\sim 10,000 \text{ km s}^{-1}$ , the interaction will occur in the early 2017.

## 6 Conclusion

In this report, we present the  $JHK_s$ -band light curves of SN 2012dn exhibited maxima with unusually long durations. The color exhibited a strong NIR excess from 30 days after the  $B$ -band maximum. None of these phenomena have previously been detected among SC SNe Ia so far, nor normal SNe Ia.

NIR light curves subtracted by those of SN 2009dc displayed flat evolutions, indicating a NIR echo from the surrounding dust shell to the SN. The fitting of the SEDs was performed using a dust emission model with amorphous carbon and a maximum

grain size of  $0.01 \mu\text{m}$ . The dust mass evolution also exhibited a plateau phase between  $t = 60$  and 110 d. Comparison of the subtracted light curve with the theoretical model provided a dust mass of  $5.5 \times 10^{-4} - 1.5 \times 10^{-3} M_\odot$  and a distance of  $4.8 - 6.0 \times 10^{-2}$  pc, suggesting the presence of circumstellar material in the pre-explosion system.

If the pre-explosion system had a wind of velocity of  $10-100 \text{ km s}^{-1}$ , the mass loss rate is estimated to be  $10^{-6} - 10^{-5} M_\odot \text{ yr}^{-1}$ , which is well consistent with those measured in Galactic recurrent novae. The light curve and color evolution comparisons indicate that SN 2012dn should belong to the class of SC SNe, while the total ejecta mass could be  $1.8-2.2 M_\odot$ . We conclude that a SC SN should originate from a WD explosion in the single-degenerate scenario.

## Acknowledgments

This work was supported by the Optical and Near-infrared Astronomy Inter-University Cooperation Program, and the Hirao Taro Foundation of the Konan University Association for Academic Research. This work was partly supported by the Grant-in-Aid for Scientific Research from JSPS (26800100) and MEXT (24103003). The works by K.M., N.T., and M.T. are partly supported by World Premier International Research Center Initiative (WPI Initiative), MEXT, Japan.

## Appendix 1 Estimate of the ejecta mass

The total ejecta mass was estimated with a scaling method using Arnett's rule (Arnett 1982) by comparison with a normal SN Ia. The slower light curve evolution indicates a greater ejecta mass if the line velocities are similar. The line velocity of SN 2012dn was almost the same as that of a low-velocity SN Ia at a similar epoch while the light curve evolutions were much slower. This suggests that the total ejecta mass could be significantly larger than that of a normal SN Ia.

Tanaka et al. (2011) presented an ejecta mass of  $\sim 1.4 M_\odot$  and kinetic energy  $\sim 1.3 \times 10^{51} \text{ erg s}^{-1}$  for normal SN 2003du. These ejecta properties were adopted as zero points in the scaling method. The velocities obtained by the same absorption lines were used for the scaling. We adopt the S II velocities, since the S II line formation region was located in the inner part of the ejecta compared with that of Si II (see Fig. 7). The line velocities of these SNe were derived as  $v_{\text{S II}, 12\text{dn}} \sim 9500 \text{ km s}^{-1}$  and  $v_{\text{S II}, 03\text{du}} \sim 9000 \text{ km s}^{-1}$  at the  $t = 5$  d. Arnett's rule is defined as,

$$\tau \propto M_{ej}^{3/4} \cdot E_K^{-1/4}, \quad (\text{A1})$$

$$v \propto M_{ej}^{-1/2} \cdot E_K^{1/2}. \quad (\text{A2})$$

Here,  $\tau$  is the timescale of the light curve and  $v$  is the expansion velocity. The light curve timescale was adopted to describe the decline rate of the  $B$ -band light curves. The ratio was given as  $\tau_{12\text{dn}} \sim 1.08$  and  $\tau_{03\text{du}} \sim 0.83$  from the inverse of the

$\Delta m_{15}(B)_{12dn} = 0.92$  and  $\Delta m_{15}(B)_{03du} = 1.02$  (corresponding to the stretch factors). The total ejecta mass was estimated to be  $M_{ej,12dn} \sim 1.8M_{\odot}$  from  $M_{ej,03du} = 1.4M_{\odot}$ . The total ejected mass significantly exceeds the Chandrasekhar-limiting mass of the WD.

A cross check was performed using scaling from the parameters of another SC SN 2009dc. An ejecta mass of  $\sim 2.4M_{\odot}$  and  $E_k = 0.9 \times 10^{51}$  erg  $s^{-1}$  were adopted as zero points (Kamiya et al. 2012). The line velocity of S II at  $t = 5$  d was measured to be  $\sim 6000$  km  $s^{-1}$  (Yamanaka et al. 2009) and the decline rate was  $\Delta m_{15}(B) \sim 0.7$  (Yamanaka et al. 2009; Silverman et al. 2011; Taubenberger et al. 2011). The total ejecta mass of SN 2012dn was estimated to be  $\sim 2.2M_{\odot}$ , which is slightly larger than that estimated above.

## References

- Altavilla, G., et al. 2004, MNRAS, 349, 1344  
 Andrews, J. E., et al. 2011, AJ, 142, 45  
 Arnett, W. D. 1982, ApJ, 253, 785  
 Bessell, M. S. 1990, PASP, 102, 1181  
 Bock, G., Parrent, J. T., & Howell, D. A. 2012, Central Bureau Electronic Telegrams, 3174  
 Bode, M. F., & Evans, A. 1980, MNRAS, 193, 21P  
 Bode, M. F., Harman, D. J., O'Brien, T. J., Bond, H. E., Starrfield, S., Darnley, M. J., Evans, A., & Eyres, S. P. S. 2007, ApJL, 665, L63  
 Branch, D., Fisher, A., & Nugent, P. 1993, AJ, 106, 2383  
 Brown, P. J. 2014, ApJL, 796, L18  
 Brown, P. J., et al. 2014, ApJ, 787, 29  
 Cappellaro, E., et al. 2001, ApJL, 549, L215  
 Chakradhari, N. K., Sahu, D. K., Srivastav, S., & Anupama, G. C. 2014, MNRAS, 443, 1663  
 Chevalier, R. A. 1986, ApJ, 308, 225  
 Crotts, A. P. S. 2015, ApJL, 804, L37  
 Dhawan, S., Leibundgut, B., Spyromilio, J., & Maguire, K. 2015, MNRAS, 448, 1345  
 Di Carlo, E., et al. 2008, ApJ, 684, 471  
 Dilday, B., et al. 2012, Science, 337, 942  
 Drozdov, D., Leising, M. D., Milne, P. A., Percy, J., Riess, A. G., Macri, L. M., Bryngelson, G. L., & Garnavich, P. M. 2015, ApJ, 805, 71  
 Dwek, E. 1983, ApJ, 274, 175  
 Dwek, E., et al. 1983, ApJ, 274, 168  
 Folatelli, G., et al. 2010, AJ, 139, 120  
 Fox, O., et al. 2009, ApJ, 691, 650  
 Fox, O. D., Filippenko, A. V., Skrutskie, M. F., Silverman, J. M., Ganeshalingam, M., Cenko, S. B., & Clubb, K. I. 2013, AJ, 146, 2  
 Fox, O. D., et al. 2016, ApJL, 816, L13  
 Friedman, A. S., et al. 2015, ApJS, 220, 9  
 Fukugita, M., Ichikawa, T., Gunn, J. E., Doi, M., Shimasaku, K., & Schneider, D. P. 1996, AJ, 111, 1748  
 Gall, C., et al. 2014, Nature, 511, 326  
 Gerardy, C. L., Fesen, R. A., Höflich, P., & Wheeler, J. C. 2000, AJ, 119, 2968  
 Hachinger, S., Mazzali, P. A., Taubenberger, S., Fink, M., Pakmor, R., Hillebrandt, W., & Seitzzahl, I. R. 2012, MNRAS, 427, 2057  
 Hachisu, I., & Kato, M. 2001, ApJ, 558, 323  
 Hachisu, I., Kato, M., Kato, T., & Matsumoto, K. 2000, ApJL, 528, L97  
 Hachisu, I., Kato, M., Nomoto, K., & Umeda, H. 1999, ApJ, 519, 314  
 Hachisu, I., Kato, M., Saio, H., & Nomoto, K. 2012, ApJ, 744, 69  
 Hamuy, M., et al. 2003, Nature, 424, 651  
 Hicken, M., Garnavich, P. M., Prieto, J. L., Blondin, S., DePoy, D. L., Kirshner, R. P., & Parrent, J. 2007, ApJL, 669, L17  
 Hillebrandt, W., Sim, S. A., & Röpke, F. K. 2007, A&A, 465, L17  
 Howell, D. A., et al. 2006, Nature, 443, 308  
 Hsiao, E. Y., Conley, A., Howell, D. A., Sullivan, M., Pritchett, C. J., Carlberg, R. G., Nugent, P. E., & Phillips, M. M. 2007, ApJ, 663, 1187  
 Iben, Jr., I., & Tutukov, A. V. 1984, ApJS, 54, 335  
 Ishiguro, M., et al. 2015, ApJL, 798, L34  
 Isogai, M., Arai, A., Yonehara, A., Kawakita, H., Uemura, M., & Nogami, D. 2015, PASJ, 67, 7  
 Itoh, R., et al. 2013, ApJL, 768, L24  
 —. 2014, PASJ, 66, 108  
 Jack, D., Hauschildt, P. H., & Baron, E. 2012, A&A, 538, A132  
 Kamiya, Y., Tanaka, M., Nomoto, K., Blinnikov, S. I., Sorokina, E. I., & Suzuki, T. 2012, ApJ, 756, 191  
 Kawabata, K. S., Hirata, R., Ikeda, Y., Akitaya, H., Seki, M., Matsumura, M., & Okazaki, A. 2000, ApJ, 540, 429  
 Kawabata, K. S., et al. 2008, in Society of Photo-Optical Instrumentation Engineers (SPIE) Conference Series, Vol. 7014, Society of Photo-Optical Instrumentation Engineers (SPIE) Conference Series  
 Kelly, P. L., et al. 2014, ApJ, 790, 3  
 Kotani, T., et al. 2005, Nuovo Cimento C Geophysics Space Physics C, 28, 755  
 Krisciunas, K., et al. 2004, AJ, 128, 3034  
 Kuroda, D., et al. 2015, ApJ, 814, 156  
 Landolt, A. U. 1992, AJ, 104, 340  
 Levanon, N., Soker, N., & García-Berro, E. 2015, MNRAS, 447, 2803  
 Li, W., et al. 2011, Nature, 480, 348  
 Maeda, K., & Iwamoto, K. 2009, MNRAS, 394, 239  
 Maeda, K., Kawabata, K., Li, W., Tanaka, M., Mazzali, P. A., Hattori, T., Nomoto, K., & Filippenko, A. V. 2009, ApJ, 690, 1745  
 Maeda, K., Nozawa, T., Nagao, T., & Motohara, K. 2015, MNRAS, 452, 3281  
 Maeda, K., et al. 2013, ApJ, 776, 5  
 Marion, G. H., et al. 2016, ApJ, 820, 92  
 Mattila, S., et al. 2008, MNRAS, 389, 141  
 Nagayama, T., et al. 2003, in Society of Photo-Optical Instrumentation Engineers (SPIE) Conference Series, Vol. 4841, Instrument Design and Performance for Optical/Infrared Ground-based Telescopes, ed. M. Iye & A. F. M. Moorwood, 459–464  
 Nomoto, K. 1982, ApJ, 253, 798  
 Nomoto, K., Thielemann, F., & Yokoi, K. 1984, ApJ, 286, 644  
 Nozawa, T., Kozasa, T., Umeda, H., Maeda, K., & Nomoto, K. 2003, ApJ, 598, 785  
 Nozawa, T., Maeda, K., Kozasa, T., Tanaka, M., Nomoto, K., & Umeda, H. 2011, ApJ, 736, 45  
 Nugent, P. E., et al. 2011, Nature, 480, 344  
 Ohtani, H., et al. 1998, in Society of Photo-Optical Instrumentation Engineers (SPIE) Conference Series, Vol. 3355, Optical Astronomical Instrumentation, ed. S. D'Odorico, 750–761  
 Pakmor, R., Kromer, M., Röpke, F. K., Sim, S. A., Ruiter, A. J., & Hillebrandt, W. 2010, Nature, 463, 61

- Pakmor, R., Kromer, M., Taubenberger, S., Sim, S. A., Röpke, F. K., & Hillebrandt, W. 2012, *ApJL*, 747, L10
- Parrent, J. T., & Howell, D. A. 2012, *Central Bureau Electronic Telegrams*, 3174, 2
- Parrent, J. T., et al. 2016, *MNRAS*
- Patat, F. 2005, *MNRAS*, 357, 1161
- Patat, F., Benetti, S., Cappellaro, E., & Turatto, M. 2006, *MNRAS*, 369, 1949
- Patat, F., et al. 2007, *Science*, 317, 924
- Perlmutter, S., et al. 1999, *ApJ*, 517, 565
- Persson, S. E., Murphy, D. C., Krzeminski, W., Roth, M., & Rieke, M. J. 1998, *AJ*, 116, 2475
- Pfannes, J. M. M., Niemeyer, J. C., & Schmidt, W. 2010, *A&A*, 509, A75
- Phillips, M. M. 1993, *ApJL*, 413, L105
- Phillips, M. M., Lira, P., Suntzeff, N. B., Schommer, R. A., Hamuy, M., & Maza, J. 1999, *AJ*, 118, 1766
- Pozzo, M., Meikle, W. P. S., Fassia, A., Geballe, T., Lundqvist, P., Chugai, N. N., & Sollerman, J. 2004, *MNRAS*, 352, 457
- Prieto, J. L., Rest, A., & Suntzeff, N. B. 2006, *ApJ*, 647, 501
- Quinn, J. L., Garnavich, P. M., Li, W., Panagia, N., Riess, A., Schmidt, B. P., & Della Valle, M. 2006, *ApJ*, 652, 512
- Riess, A. G., et al. 1998, *AJ*, 116, 1009
- Sakon, I., et al. 2009, *ApJ*, 692, 546
- Scalzo, R., et al. 2012, *ApJ*, 757, 12
- Scalzo, R. A., et al. 2010, *ApJ*, 713, 1073
- Schaefer, B. E. 1987, *ApJL*, 323, L47
- Schlafly, E. F., & Finkbeiner, D. P. 2011, *ApJ*, 737, 103
- Silverman, J. M., Ganeshalingam, M., Li, W., Filippenko, A. V., Miller, A. A., & Poznanski, D. 2011, *MNRAS*, 410, 585
- Simon, J. D., et al. 2009, *ApJ*, 702, 1157
- Sollerman, J., et al. 2004, *A&A*, 428, 555
- Sparks, W. B., Macchetto, F., Panagia, N., Boffi, F. R., Branch, D., Hazen, M. L., & Della Valle, M. 1999, *ApJ*, 523, 585
- Stanishev, V., et al. 2007, *A&A*, 469, 645
- Stetson, P. B. 1987, *PASP*, 99, 191
- Stritzinger, M., Mazzali, P. A., Sollerman, J., & Benetti, S. 2006, *A&A*, 460, 793
- Tanaka, M., Mazzali, P. A., Stanishev, V., Maurer, I., Kerzendorf, W. E., & Nomoto, K. 2011, *MNRAS*, 410, 1725
- Tanaka, M., et al. 2010, *ApJ*, 714, 1209
- Tanikawa, A., Nakasato, N., Sato, Y., Nomoto, K., Maeda, K., & Hachisu, I. 2015, *ApJ*, 807, 40
- Taubenberger, S., et al. 2011, *MNRAS*, 61
- Theureau, G., Bottinelli, L., Coudreau-Durand, N., Gouguenheim, L., Hallet, N., Loulergue, M., Paturel, G., & Teerikorpi, P. 1998, *A&AS*, 130, 333
- Wang, L. 2005, *ApJL*, 635, L33
- Wang, X., Li, W., Filippenko, A. V., Foley, R. J., Smith, N., & Wang, L. 2008, *ApJ*, 677, 1060
- Wang, X., Wang, L., Pain, R., Zhou, X., & Li, Z. 2006, *ApJ*, 645, 488
- Wang, X., et al. 2009, *ApJ*, 697, 380
- Watanabe, M., Takahashi, Y., Sato, M., Watanabe, S., Fukuhara, T., Hamamoto, K., & Ozaki, A. 2012, in *Society of Photo-Optical Instrumentation Engineers (SPIE) Conference Series*, Vol. 8446, *Society of Photo-Optical Instrumentation Engineers (SPIE) Conference Series*
- Webbink, R. F. 1984, *ApJ*, 277, 355
- Woudt, P. A., et al. 2009, *ApJ*, 706, 738
- Yamanaka, M., et al. 2009, *ApJL*, 707, L118
- . 2014, *ApJL*, 782, L35
- . 2015, *ApJ*, 806, 191
- Yanagisawa, K., Kuroda, D., Yoshida, M., Shimizu, Y., Nagayama, S., Toda, H., Ohta, K., & Kawai, N. 2010, in *American Institute of Physics Conference Series*, Vol. 1279, *American Institute of Physics Conference Series*, ed. N. Kawai & S. Nagataki, 466–468
- Yatsu, Y., et al. 2015, *ApJ*, 802, 84
- Yoon, S.-C., Podsiadlowski, P., & Rosswog, S. 2007, *MNRAS*, 380, 933
- Yoshida, M. 2005, *Journal of Korean Astronomical Society*, 38, 117
- Yuan, F., et al. 2010, *ApJ*, 715, 1338

**Table 1.** Summary of the properties of the telescopes, instruments, and observatories.

Observatory	Telescope	Instruments	Filters/Resolutions	Number of nights
NO <sup>a</sup>	1.6m Pirka	MSI <sup>b</sup>	$U, B, V, R, I$	44
			$R = 150$	3
AO <sup>c</sup>	0.5m MITSuME <sup>d</sup>	CCD	$g', R, I$	11
KAO <sup>e</sup>	1.3m Araki	Adler <sup>f</sup>	$B, V, I, g', i', z'$	24
OKUAO <sup>g</sup>	0.5m	Andor CCD	$B, V, R, I$	15
		ST10 CCD	$B, V, R, I$	14
OAO <sup>h</sup>	0.5m MITSuME <sup>d</sup>	CCD	$g', R, I$	67
		188cm	KOOLS <sup>i</sup>	$B, V, R, I$
NHAO <sup>j</sup>	2.0m Nayuta	NIC <sup>k</sup>	$J, H, K_s$	21
HHO <sup>l</sup>	1.5m Kanata	HOWPol <sup>m</sup>	$B, V, R, I, z' + Y$	52
			$R = 400$	30
IO <sup>n</sup>	1.0m	IR Cam	$J, H, K_s$	24
IAO <sup>o</sup>	1.05m MITSuME <sup>d</sup>	CCD	$g', R, I$	29
SAAO <sup>p</sup>	1.4m IRSF	SIRIUS <sup>q</sup>	$J, H, K_s$	80

**Note.** <sup>a</sup>Nayoro Observatory; <sup>b</sup>Multispectral Imager (Watanabe et al. 2012); <sup>c</sup>Akeno Observatory; <sup>d</sup>Multicolor Imaging Telescopes for Survey and Monstrous Explosions (Kotani et al. 2005); <sup>e</sup>Koyama Astronomical Observatory; <sup>f</sup>Araki telescope Dual-band imagER (Isogai et al. 2015); <sup>g</sup>Osaka Kyoiku University Astronomical Observatory; <sup>h</sup>Okayama Astrophysical Observatory; <sup>i</sup>Kyoto Okayama Optical Low-dispersion Spectrograph (Ohtani et al. 1998); <sup>j</sup>Nishi-Harima Astronomical Observatory; <sup>k</sup>Nishi-harima Infrared Camera; <sup>l</sup>Higashi-Hiroshima Observatory; <sup>m</sup>Hiroshima One-shot Wide-field Polarimeter (Kawabata et al. 2008); <sup>n</sup>Iriki Observatory; <sup>o</sup>Ishigaki-jima Astronomical Observatory; <sup>p</sup>South African Astronomical Observatory; <sup>q</sup>Near-infrared simultaneous three-band camera (Nagayama et al. 2003)

**Table 2.** MSI photometry of SN 2012dn in the *UBVRI* bands

MJD	Phase	<i>U</i>	<i>B</i>	<i>V</i>	<i>R</i>	<i>I</i>
56122.6	-9.79	14.513(0.098)	15.172(0.016)	15.005(0.013)	14.974(0.025)	14.879(0.025)
56123.6	-8.79	14.379(0.098)	14.990(0.016)	14.856(0.011)	14.841(0.025)	14.759(0.026)
56124.6	-7.79	14.262(0.100)	14.881(0.017)	14.747(0.013)	14.726(0.035)	14.666(0.026)
56125.6	-6.79	14.169(0.101)	14.797(0.017)	14.640(0.012)	14.639(0.025)	14.596(0.031)
56126.6	-5.79	14.142(0.099)	14.597(0.020)	14.438(0.017)	...	...
56128.6	-3.79	14.009(0.099)	14.551(0.020)	14.448(0.012)	14.442(0.025)	14.429(0.025)
56129.6	-2.79	...	...	14.373(0.025)	...	...
56131.6	-0.79	13.999(0.099)	14.532(0.017)	14.360(0.012)	14.334(0.025)	14.360(0.036)
56136.6	4.21	14.298(0.102)	14.543(0.017)	14.309(0.012)	...	...
56137.7	5.31	...	...	14.344(0.019)	...	...
56138.6	6.21	14.321(0.110)	14.630(0.017)	14.373(0.013)	14.357(0.026)	14.373(0.040)
56142.6	10.21	...	...	14.456(0.049)	...	...
56145.6	13.21	...	...	14.501(0.013)	...	...
56146.5	14.11	15.069(0.098)	15.249(0.017)	14.542(0.012)	...	...
56147.6	15.21	15.203(0.099)	15.326(0.017)	14.603(0.012)	14.504(0.025)	14.320(0.027)
56148.6	16.21	15.339(0.099)	15.487(0.017)	14.694(0.018)	14.575(0.025)	14.370(0.026)
56150.5	18.11	15.635(0.100)	15.677(0.017)	14.778(0.016)	14.631(0.026)	14.378(0.026)
56153.5	21.11	16.031(0.109)	16.009(0.020)	14.958(0.013)	14.701(0.025)	14.357(0.026)
56155.5	23.11	16.302(0.100)	16.226(0.016)	15.110(0.011)	14.784(0.025)	14.377(0.025)
56157.6	25.21	16.298(0.141)	16.412(0.018)	15.145(0.012)	...	...
56160.5	28.11	16.622(0.195)	16.639(0.016)	15.299(0.012)	...	...
56161.5	29.11	16.873(0.100)	16.719(0.018)	15.350(0.012)	...	...
56166.5	34.11	16.950(0.120)	16.957(0.020)	15.552(0.023)	...	...
56167.5	35.11	...	17.102(0.104)	...	...	...
56169.5	37.11	...	16.959(0.155)	15.574(0.024)	...	...
56171.6	39.21	...	17.114(0.043)	15.713(0.016)	...	...
56172.6	40.21	16.874(0.186)	17.136(0.023)	15.767(0.015)	...	...
56173.5	41.11	...	17.117(0.021)	15.767(0.013)	...	...
56174.5	42.11	...	17.265(0.091)	15.823(0.013)	...	...
56175.5	43.11	17.431(0.123)	17.256(0.017)	15.856(0.013)	...	...
56177.5	45.11	16.618(0.293)	17.253(0.017)	16.037(0.013)	15.609(0.030)	15.094(0.029)
56182.6	50.21	...	17.309(0.033)	16.028(0.014)	...	...
56184.5	52.11	17.519(0.131)	17.474(0.027)	16.104(0.013)	...	...
56187.5	55.11	...	...	16.074(0.039)	...	...
56188.5	56.11	17.861(0.274)	17.612(0.022)	16.207(0.019)	...	...
56189.5	57.11	...	17.043(0.275)	16.191(0.025)	...	...
56190.5	58.11	17.887(0.124)	17.484(0.021)	16.412(0.014)	16.073(0.027)	15.567(0.025)
56191.6	59.21	...	...	16.270(0.052)	...	...
56202.4	70.01	...	17.852(0.042)	16.851(0.019)	16.574(0.029)	16.107(0.034)
56205.5	73.11	...	...	16.667(0.019)	...	...
56207.5	75.11	...	...	16.534(0.016)	...	...
56224.4	92.01	...	...	17.486(0.050)	17.252(0.052)	16.691(0.067)
56226.4	94.01	...	...	17.360(0.044)	...	...

Table 3. MITSuME telescope photometry of SN 2012dn in the  $g'RI$  bands

MJD	Phase	$g'$	$R$	$I$	Observatories
56120.7	-11.7	15.407(0.107)	15.366(0.088)	...	IAO
56121.7	-10.7	15.162(0.107)	15.200(0.088)	...	IAO
56123.6	-8.8	14.821(0.030)	14.806(0.031)	14.723(0.038)	OAO
56123.6	-8.8	14.830(0.031)	14.834(0.033)	14.801(0.040)	OAO
56123.7	-8.7	14.838(0.107)	14.883(0.088)	...	IAO
56124.6	-7.8	14.544(0.025)	...	...	AO
56124.7	-7.7	14.606(0.040)	14.748(0.037)	14.664(0.044)	OAO
56125.6	-6.8	14.661(0.029)	14.638(0.030)	14.570(0.033)	OAO
56125.6	-6.8	14.730(0.028)	14.616(0.030)	14.558(0.033)	OAO
56125.6	-6.8	14.636(0.027)	14.613(0.029)	14.513(0.033)	OAO
56126.6	-5.8	14.457(0.107)	14.540(0.088)	...	IAO
56126.6	-5.8	14.527(0.030)	14.531(0.032)	14.501(0.039)	OAO
56126.6	-5.8	14.540(0.031)	14.539(0.032)	14.499(0.039)	OAO
56126.6	-5.8	14.544(0.031)	14.519(0.033)	14.505(0.041)	OAO
56127.7	-4.8	14.524(0.046)	14.439(0.037)	14.444(0.045)	OAO
56127.7	-4.7	14.429(0.106)	14.511(0.087)	...	IAO
56129.7	-2.7	14.348(0.106)	14.412(0.087)	...	IAO
56131.6	-0.8	14.431(0.031)	14.334(0.030)	14.320(0.034)	OAO
56131.7	-0.7	14.404(0.032)	14.280(0.034)	14.320(0.040)	AO
56132.6	0.2	14.363(0.028)	14.320(0.029)	14.346(0.033)	OAO
56132.6	0.2	14.393(0.027)	14.316(0.028)	14.325(0.032)	OAO
56132.6	0.2	14.389(0.027)	14.304(0.028)	14.326(0.032)	OAO
56133.6	1.2	14.391(0.030)	14.285(0.029)	14.307(0.033)	OAO
56133.6	1.2	14.367(0.030)	14.304(0.028)	14.285(0.033)	OAO
56133.6	1.2	14.380(0.027)	14.303(0.028)	14.320(0.032)	OAO
56134.6	2.2	14.251(0.107)	14.284(0.088)	14.285(0.020)	IAO
56134.6	2.2	14.341(0.026)	14.278(0.028)	14.308(0.032)	OAO
56134.6	2.2	14.384(0.026)	14.293(0.028)	14.295(0.032)	OAO
56134.6	2.2	14.364(0.026)	14.287(0.028)	14.304(0.032)	OAO
56135.6	3.2	14.374(0.038)	14.312(0.030)	14.320(0.036)	OAO
56135.7	3.3	14.329(0.106)	14.332(0.087)	14.318(0.014)	IAO
56136.6	4.2	14.332(0.106)	14.325(0.087)	14.331(0.014)	IAO
56136.6	4.2	14.334(0.035)	14.298(0.030)	14.291(0.036)	OAO
56136.7	4.3	14.390(0.028)	14.286(0.029)	14.323(0.034)	OAO
56137.7	5.3	14.489(0.041)	14.354(0.033)	14.337(0.039)	OAO
56138.6	6.2	14.364(0.031)	14.325(0.031)	14.341(0.035)	OAO
56138.6	6.2	14.493(0.032)	14.272(0.030)	14.343(0.034)	OAO
56138.6	6.2	14.425(0.038)	14.340(0.030)	14.372(0.036)	OAO
56139.5	7.1	14.762(0.077)	14.377(0.057)	14.453(0.079)	OAO
56139.6	7.2	14.415(0.071)	14.262(0.032)	14.181(0.033)	AO
56141.6	9.2	...	14.286(0.064)	14.187(0.033)	AO
56141.7	9.3	14.578(0.035)	14.383(0.031)	14.328(0.036)	OAO
56142.6	10.2	14.500(0.031)	14.383(0.030)	14.378(0.034)	OAO
56142.7	10.3	14.560(0.030)	14.409(0.028)	14.336(0.034)	OAO
56142.7	10.3	14.602(0.031)	14.343(0.029)	14.358(0.032)	OAO
56143.6	11.2	14.644(0.026)	14.393(0.028)	14.361(0.031)	OAO
56143.6	11.2	14.651(0.027)	14.390(0.028)	14.329(0.031)	OAO
56143.6	11.2	14.648(0.026)	14.394(0.028)	14.327(0.030)	OAO
56145.6	13.2	14.749(0.027)	14.437(0.030)	14.348(0.035)	AO
56145.6	13.2	14.755(0.028)	14.442(0.029)	14.434(0.032)	OAO
56145.6	13.2	14.757(0.028)	14.439(0.028)	14.392(0.032)	OAO
56146.6	14.2	14.878(0.038)	14.397(0.036)	14.252(0.046)	AO
56147.6	15.2	14.898(0.035)	14.542(0.031)	14.414(0.036)	OAO
56147.6	15.2	14.932(0.034)	14.538(0.030)	14.394(0.034)	OAO
56147.7	15.3	14.954(0.106)	14.566(0.087)	14.346(0.016)	IAO
56148.6	16.2	14.985(0.038)	14.559(0.031)	14.370(0.036)	OAO
56148.6	16.2	15.013(0.043)	14.571(0.033)	14.392(0.037)	OAO
56148.6	16.2	14.961(0.041)	14.548(0.032)	14.366(0.038)	OAO
56150.7	18.3	15.169(0.038)	14.594(0.031)	14.391(0.036)	OAO
56151.6	19.2	15.288(0.106)	14.662(0.087)	14.364(0.014)	IAO
56152.7	20.3	15.432(0.106)	14.721(0.087)	14.353(0.012)	IAO
56153.5	21.1	15.496(0.106)	14.749(0.088)	14.333(0.015)	IAO
56154.6	22.2	15.607(0.031)	14.737(0.029)	14.379(0.032)	OAO
56154.6	22.2	15.540(0.032)	14.718(0.028)	14.400(0.032)	OAO
56154.6	22.2	15.557(0.031)	14.747(0.029)	14.389(0.034)	OAO
56155.6	23.2	15.633(0.030)	14.789(0.029)	14.388(0.032)	OAO
56155.6	23.2	15.681(0.031)	14.755(0.028)	14.393(0.031)	OAO
56155.6	23.2	15.692(0.030)	14.778(0.028)	14.389(0.031)	OAO
56156.6	24.2	15.729(0.036)	14.793(0.029)	14.409(0.032)	OAO
56156.6	24.2	15.799(0.038)	14.816(0.029)	14.437(0.033)	OAO
56156.6	24.2	15.726(0.040)	14.828(0.030)	14.414(0.032)	OAO
56158.6	26.2	15.931(0.033)	14.914(0.028)	14.448(0.031)	OAO
56158.6	26.2	15.955(0.107)	14.848(0.088)	14.416(0.014)	IAO
56158.6	26.2	15.901(0.031)	14.916(0.029)	14.435(0.032)	OAO
56158.6	26.2	15.920(0.031)	14.867(0.028)	14.448(0.031)	OAO
56159.6	27.2	15.995(0.033)	14.930(0.029)	14.478(0.032)	OAO
56159.6	27.2	16.075(0.106)	14.962(0.087)	14.473(0.012)	IAO
56159.6	27.2	15.983(0.031)	14.946(0.029)	14.491(0.032)	OAO
56159.6	27.2	16.043(0.034)	14.927(0.029)	14.484(0.032)	OAO
56160.6	28.2	16.061(0.039)	14.992(0.030)	14.537(0.033)	OAO



Table 3. (Continued)

MJD	Phase	$g'$	$R$	$I$	Observatories
56160.6	28.2	16.064(0.035)	14.980(0.030)	14.523(0.034)	OAO
56160.6	28.2	16.099(0.042)	14.997(0.030)	14.526(0.034)	OAO
56164.7	32.3	16.245(0.039)	15.138(0.030)	14.620(0.032)	OAO
56165.6	33.2	16.238(0.036)	15.153(0.030)	14.662(0.033)	OAO
56169.6	37.2	16.682(0.127)	15.217(0.035)	14.803(0.040)	OAO
56171.5	39.1	16.632(0.106)	15.460(0.087)	...	IAO
56172.6	40.2	16.626(0.106)	15.453(0.087)	...	IAO
56173.5	41.1	16.197(0.108)	15.351(0.064)	14.686(0.066)	AO
56174.6	42.2	16.576(0.107)	15.470(0.087)	14.844(0.014)	IAO
56178.6	46.2	16.694(0.057)	15.643(0.034)	15.154(0.041)	OAO
56178.6	46.2	16.856(0.107)	15.759(0.087)	15.146(0.013)	IAO
56179.5	47.1	16.884(0.107)	15.800(0.088)	15.191(0.014)	IAO
56180.5	48.1	16.512(0.069)	...	...	AO
56182.5	50.1	16.943(0.107)	15.901(0.088)	15.293(0.014)	IAO
56182.5	50.1	16.659(0.093)	15.857(0.046)	15.225(0.044)	OAO
56183.5	51.1	16.943(0.107)	15.947(0.087)	15.309(0.014)	IAO
56184.5	52.1	16.966(0.107)	15.947(0.087)	15.306(0.014)	IAO
56187.6	55.2	17.054(0.107)	16.053(0.087)	15.521(0.014)	IAO
56191.5	59.1	17.210(0.107)	16.280(0.088)	15.639(0.014)	IAO
56224.5	92.1	17.925(0.111)	17.611(0.092)	17.087(0.031)	IAO
56226.5	94.1	18.012(0.109)	17.721(0.090)	17.160(0.026)	IAO
56238.5	106.1	18.129(0.113)	17.962(0.097)	17.587(0.056)	IAO
56239.5	107.1	18.235(0.115)	18.090(0.096)	17.745(0.054)	IAO

Table 4. Araki telescope photometry of SN 2012dn in the  $g'i'z'$   $BVI$  bands

MJD	Phase	$B$	$V$	$I$	$g'$	$i'$	$z'$
56125.7	-6.7	14.598(0.019)	14.544(0.011)	14.513(0.012)	14.523(0.014)	14.829(0.011)	14.988(0.000)
56126.7	-5.7	14.511(0.019)	14.454(0.015)	14.454(0.016)	14.445(0.015)	14.790(0.012)	14.931(0.000)
56131.7	-0.7	14.341(0.020)	14.269(0.014)	14.282(0.012)	14.248(0.015)	14.621(0.011)	14.650(0.000)
56132.7	0.3	14.355(0.032)	14.346(0.036)	14.260(0.041)	14.240(0.017)	14.607(0.012)	14.622(0.001)
56133.6	1.2	14.393(0.052)	14.201(0.025)	14.258(0.033)	14.251(0.015)	14.618(0.012)	14.478(0.003)
56134.7	2.3	14.359(0.021)	14.254(0.013)	14.264(0.012)	14.260(0.015)	14.613(0.013)	14.582(0.000)
56135.7	3.3	14.374(0.021)	14.215(0.016)	14.255(0.012)	14.254(0.014)	14.603(0.010)	14.568(0.000)
56138.6	6.2	14.461(0.019)	14.275(0.012)	14.265(0.012)	14.305(0.014)	14.618(0.010)	14.511(0.000)
56139.6	7.2	14.519(0.019)	14.286(0.013)	14.252(0.018)	14.335(0.016)	14.606(0.014)	14.481(0.000)
56140.7	8.3	14.577(0.019)	14.313(0.012)	14.263(0.016)	14.371(0.015)	14.625(0.013)	14.456(0.001)
56141.6	9.2	14.668(0.036)	14.350(0.015)	14.227(0.034)	14.424(0.018)	14.630(0.017)	14.444(0.003)
56142.6	10.2	14.730(0.020)	14.368(0.012)	14.276(0.014)	14.466(0.015)	14.656(0.012)	14.461(0.000)
56143.6	11.2	14.797(0.019)	14.380(0.012)	14.296(0.012)	14.505(0.015)	14.645(0.012)	14.439(0.000)
56145.6	13.2	14.983(0.020)	14.449(0.016)	14.304(0.013)	14.647(0.015)	14.682(0.012)	14.420(0.000)
56146.6	14.2	15.088(0.019)	14.492(0.017)	14.320(0.012)	14.722(0.015)	14.691(0.015)	14.420(0.000)
56147.6	15.2	15.195(0.020)	14.549(0.012)	14.328(0.011)	14.792(0.015)	14.704(0.012)	14.433(0.000)
56148.6	16.2	15.299(0.020)	14.598(0.011)	14.320(0.013)	14.877(0.015)	14.713(0.012)	14.426(0.000)
56163.6	31.2	16.584(0.024)	15.436(0.012)	14.535(0.011)	16.081(0.018)	14.934(0.011)	14.660(0.000)
56174.6	42.2	...	15.903(0.025)	14.923(0.013)	16.590(0.039)	15.344(0.015)	15.025(0.000)
56181.5	49.1	17.200(0.031)	16.084(0.017)	15.191(0.012)	16.747(0.018)	15.648(0.012)	15.291(0.000)
56183.5	51.1	...	16.076(0.040)	15.234(0.019)	16.794(0.036)	15.717(0.013)	15.376(0.000)
56196.5	64.1	...	16.593(0.018)	15.805(0.016)	17.095(0.022)	16.280(0.015)	15.976(0.000)
56197.5	65.1	...	...	...	...	...	15.947(0.000)
56198.5	66.1	...	...	...	...	...	16.075(0.001)

Table 5. OKU 51cm telescope photometry of SN 2012dn in the  $BVRI$  bands

MJD	Phase	$B$	$V$	$R$	$I$	Instruments
56123.6	-8.8	15.024(0.022)	...	14.052(0.025)	...	ST10
56124.7	-7.7	14.791(0.030)	14.740(0.023)	14.696(0.025)	14.655(0.036)	ST10
56125.6	-6.8	14.708(0.020)	14.659(0.019)	14.631(0.028)	14.594(0.029)	ST10
56126.6	-5.8	14.641(0.025)	14.413(0.011)	14.541(0.036)	14.532(0.028)	ST10
56131.6	-0.8	14.442(0.022)	14.392(0.021)	14.356(0.065)	14.279(0.137)	ST10
56132.7	0.3	14.578(0.058)	14.364(0.023)	14.363(0.050)	14.364(0.036)	ST10
56133.6	1.2	...	14.381(0.011)	14.286(0.095)	14.339(0.027)	ST10
56134.7	2.3	...	14.369(0.021)	14.306(0.030)	14.344(0.040)	ST10
56136.6	4.2	...	14.392(0.038)	14.346(0.039)	...	Andor
56137.7	5.3	...	14.373(0.075)	...	...	Andor
56141.7	9.3	...	14.431(0.033)	14.408(0.042)	...	Andor
56142.6	10.2	14.782(0.030)	14.495(0.017)	14.402(0.026)	14.354(0.028)	Andor
56143.6	11.2	14.892(0.042)	14.510(0.025)	14.597(0.171)	...	Andor
56146.6	14.2	15.236(0.023)	14.627(0.016)	14.510(0.030)	14.368(0.026)	Andor
56147.7	15.3	15.288(0.027)	14.679(0.016)	14.553(0.030)	14.378(0.034)	Andor
56154.6	22.2	16.198(0.035)	15.069(0.031)	14.756(0.028)	14.367(0.028)	Andor
56155.6	23.2	...	15.126(0.024)	14.782(0.040)	14.378(0.028)	ST10
56156.6	24.2	...	...	14.780(0.026)	14.414(0.026)	Andor
56158.6	26.2	...	15.293(0.025)	14.895(0.029)	14.442(0.037)	ST10
56159.6	27.2	...	15.240(0.046)	...	...	ST10
56161.6	29.2	...	...	...	14.415(0.278)	ST10
56164.6	32.2	...	...	15.058(0.027)	...	Andor
56165.6	33.2	...	...	15.093(0.026)	14.644(0.027)	Andor
56174.6	42.2	...	...	15.404(0.050)	...	Andor

Table 6. HOWPol photometry of SN 2012dn in the *UBVRI* bands

MJD	Phase	<i>B</i>	<i>V</i>	<i>R</i>	<i>I</i>	<i>z'</i> + <i>Y</i>
56131.6	-0.8	14.425(0.036)	14.303(0.029)	14.314(0.041)	14.341(0.048)	14.777(0.068)
56132.6	0.2	14.439(0.028)	14.316(0.024)	14.300(0.041)	14.323(0.038)	14.719(0.062)
56133.7	1.3	14.461(0.028)	14.305(0.023)	14.274(0.035)	14.302(0.038)	14.677(0.065)
56134.7	2.3	14.481(0.050)	14.337(0.029)	14.278(0.056)	14.322(0.053)	14.668(0.069)
56135.7	3.3	...	14.526(0.126)	14.298(0.073)	14.399(0.085)	14.746(0.078)
56137.5	5.1	14.623(0.089)	14.389(0.091)	14.291(0.039)	14.294(0.041)	14.631(0.064)
56138.6	6.2	14.668(0.056)	14.366(0.034)	14.349(0.033)	14.294(0.045)	14.680(0.086)
56139.6	7.2	14.687(0.045)	14.382(0.040)	14.286(0.034)	14.334(0.055)	14.581(0.078)
56140.6	8.2	14.792(0.047)	14.396(0.029)	14.371(0.038)	14.400(0.045)	14.652(0.070)
56141.7	9.3	14.816(0.037)	14.481(0.027)	14.370(0.044)	14.383(0.055)	14.643(0.062)
56142.6	10.2	14.926(0.060)	14.424(0.050)	14.369(0.072)	14.347(0.117)	14.616(0.081)
56143.6	11.2	15.002(0.033)	14.442(0.033)	14.417(0.034)	14.355(0.042)	14.605(0.065)
56146.5	14.1	...	14.567(0.022)	14.487(0.026)	14.368(0.025)	14.515(0.130)
56149.5	17.1	15.644(0.040)	14.696(0.047)	14.553(0.042)	14.383(0.047)	14.540(0.070)
56150.5	18.1	15.868(0.074)	14.827(0.050)	14.713(0.049)	14.577(0.058)	14.680(0.129)
56155.5	23.1	16.355(0.043)	15.009(0.030)	14.776(0.049)	14.409(0.055)	14.530(0.074)
56156.5	24.1	16.393(0.058)	15.100(0.074)	14.836(0.068)	14.536(0.056)	14.574(0.078)
56158.5	26.1	16.704(0.049)	15.271(0.033)	14.984(0.074)	14.555(0.042)	14.656(0.076)
56159.6	27.2	16.745(0.040)	15.267(0.043)	14.915(0.033)	14.508(0.042)	14.607(0.070)
56160.5	28.1	16.858(0.048)	15.302(0.030)	14.994(0.038)	14.565(0.038)	14.662(0.069)
56161.5	29.1	16.845(0.066)	15.345(0.047)	15.028(0.049)	14.624(0.036)	14.594(0.107)
56162.5	30.1	...	15.525(0.033)	...	...	...
56163.6	31.2	16.986(0.066)	15.468(0.050)	15.142(0.053)	14.602(0.057)	14.687(0.090)
56164.6	32.2	17.057(0.061)	15.487(0.053)	15.145(0.029)	14.644(0.041)	14.737(0.101)
56165.6	33.2	17.120(0.059)	15.495(0.019)	15.152(0.031)	14.689(0.027)	14.760(0.080)
56170.5	38.1	...	15.717(0.073)	15.393(0.061)	14.888(0.045)	14.893(0.071)
56172.5	40.1	17.430(0.043)	15.841(0.033)	15.498(0.043)	14.926(0.046)	15.001(0.066)
56182.5	50.1	17.649(0.058)	16.119(0.037)	15.900(0.044)	15.335(0.051)	15.336(0.071)
56184.5	52.1	17.753(0.086)	16.207(0.044)	16.001(0.043)	15.407(0.035)	15.426(0.067)
56187.5	55.1	17.702(0.066)	16.279(0.021)	16.062(0.046)	15.682(0.104)	...
56188.6	56.2	17.873(0.089)	16.276(0.031)	16.110(0.044)	15.540(0.044)	...
56193.5	61.1	17.937(0.098)	16.490(0.042)	16.348(0.039)	15.781(0.040)	15.766(0.065)
56196.5	64.1	...	16.737(0.127)	...	15.921(0.086)	15.845(0.097)
56202.5	70.1	17.902(0.066)	17.118(0.051)	...	...	16.175(0.063)
56203.5	71.1	18.019(0.092)	17.166(0.037)	...	...	...
56207.5	75.1	18.058(0.074)	16.949(0.038)	16.800(0.047)	16.308(0.047)	16.469(0.071)
56209.5	77.1	...	17.191(0.044)	17.059(0.178)	16.338(0.050)	16.491(0.076)
56211.5	79.1	...	...	16.777(0.042)	...	...
56212.4	80.0	...	17.005(0.028)	16.895(0.029)	16.417(0.039)	16.644(0.069)
56213.4	81.0	...	17.207(0.057)	17.186(0.112)	16.585(0.032)	...
56214.5	82.1	...	...	16.756(0.050)	16.607(0.054)	16.853(0.073)
56215.5	83.1	...	17.229(0.051)	17.050(0.039)	16.582(0.049)	16.671(0.073)
56216.5	84.1	...	...	16.880(0.037)	16.550(0.053)	16.696(0.078)
56220.5	88.1	...	17.454(0.058)	17.239(0.036)	16.805(0.047)	17.059(0.087)
56221.4	89.0	...	17.328(0.064)	17.096(0.061)	16.636(0.050)	16.773(0.082)
56223.4	91.0	...	17.704(0.233)	17.369(0.113)	17.069(0.093)	17.091(0.112)
56224.4	92.0	...	17.175(0.071)	17.085(0.083)	16.500(0.093)	16.894(0.118)
56225.4	93.0	...	17.259(0.084)	17.164(0.076)	16.890(0.076)	...
56226.4	94.0	...	17.354(0.076)	17.183(0.090)	...	...
56228.4	96.0	...	...	16.904(0.086)	16.676(0.068)	16.834(0.089)
56228.4	96.0	...	...	...	16.676(0.076)	16.605(0.532)
56233.4	101.0	...	...	...	17.107(0.062)	...

Table 7. NIR-band photometry of SN 2012dn

MJD	Phase	<i>J</i>	<i>H</i>	<i>K<sub>s</sub></i>	Instruments
56120.8	-11.6	15.09(0.04)	15.09(0.04)	15.04(0.09)	IRSF
56125.1	-7.3	14.62(0.03)	14.70(0.03)	14.57(0.06)	IRSF
56125.7	-6.7	14.67(0.19)	14.72(0.02)	...	NIC
56126.1	-6.3	14.56(0.03)	14.58(0.03)	14.56(0.07)	IRSF
56127.1	-5.3	14.50(0.03)	14.59(0.03)	14.58(0.08)	IRSF
56129.6	-2.8	14.68(0.02)	14.82(0.04)	...	IR Cam
56132.0	-0.4	14.34(0.03)	14.44(0.03)	14.24(0.05)	IRSF
56132.7	0.3	14.34(0.03)	...	...	IR Cam
56133.0	0.6	14.43(0.03)	14.46(0.03)	14.19(0.05)	IRSF
56133.6	1.2	14.55(0.05)	14.63(0.05)	...	IR Cam
56133.7	1.3	14.39(0.12)	14.64(0.09)	...	NIC
56133.7	1.3	...	...	14.36(0.20)	NIC
56134.0	1.6	14.42(0.03)	14.46(0.03)	14.37(0.08)	IRSF
56134.6	2.2	14.46(0.03)	14.51(0.02)	14.37(0.06)	NIC
56135.6	3.2	14.36(0.17)	14.50(0.07)	14.45(0.10)	NIC
56136.0	3.6	14.38(0.03)	14.38(0.03)	14.21(0.05)	IRSF
56136.6	4.2	14.55(0.07)	14.52(0.02)	14.43(0.08)	NIC
56137.0	4.6	14.43(0.03)	14.43(0.03)	14.37(0.05)	IRSF
56137.6	5.2	14.51(0.04)	14.48(0.03)	14.36(0.05)	NIC
56138.0	5.6	14.39(0.03)	14.34(0.03)	14.16(0.05)	IRSF
56138.6	6.2	14.56(0.01)	14.49(0.02)	14.34(0.04)	NIC
56139.0	6.6	14.40(0.03)	14.34(0.03)	14.22(0.05)	IRSF
56139.6	7.2	14.52(0.03)	14.46(0.01)	14.33(0.03)	NIC
56140.6	8.2	14.61(0.12)	14.47(0.04)	14.36(0.05)	NIC
56141.1	8.7	14.48(0.03)	14.27(0.03)	14.13(0.05)	IRSF
56141.6	9.2	14.61(0.02)	14.44(0.02)	14.26(0.04)	NIC
56142.1	9.7	14.51(0.03)	14.38(0.03)	14.25(0.06)	IRSF
56143.1	10.7	14.60(0.03)	14.41(0.03)	14.10(0.05)	IRSF
56143.6	11.2	14.71(0.02)	14.42(0.01)	14.27(0.05)	NIC
56145.6	13.2	14.80(0.03)	14.42(0.02)	14.29(0.02)	NIC
56146.7	14.3	14.80(0.06)	...	...	IR Cam
56149.1	16.7	14.73(0.04)	14.32(0.03)	14.16(0.06)	IRSF
56153.0	20.6	14.72(0.04)	14.26(0.03)	14.25(0.06)	IRSF
56156.6	24.2	14.85(0.04)	...	...	IR Cam
56159.6	27.2	14.74(0.04)	14.31(0.01)	14.22(0.04)	NIC
56161.0	28.6	14.60(0.03)	14.22(0.03)	14.13(0.04)	IRSF
56163.0	30.6	14.55(0.03)	14.21(0.03)	14.12(0.05)	IRSF
56164.6	32.2	14.73(0.00)	14.29(0.01)	14.21(0.04)	NIC
56165.6	33.2	14.73(0.01)	14.26(0.01)	14.13(0.05)	NIC
56166.9	34.5	14.64(0.03)	14.19(0.03)	14.05(0.05)	IRSF
56174.6	42.2	14.98(0.04)	14.32(0.01)	14.09(0.05)	NIC
56174.8	42.4	14.82(0.03)	14.27(0.02)	13.94(0.04)	IRSF
56175.8	43.4	14.87(0.04)	14.19(0.03)	13.89(0.04)	IRSF
56176.8	44.4	14.94(0.04)	14.24(0.03)	14.00(0.05)	IRSF
56177.7	45.3	15.01(0.04)	14.23(0.03)	13.94(0.05)	IRSF
56178.7	46.3	14.99(0.04)	14.23(0.03)	13.97(0.05)	IRSF
56180.7	48.3	15.05(0.04)	14.27(0.03)	13.85(0.04)	IRSF
56181.7	49.3	15.07(0.04)	14.28(0.03)	13.86(0.05)	IRSF
56182.6	50.2	15.55(0.05)	...	...	IR Cam
56182.7	50.3	15.25(0.05)	14.27(0.03)	13.80(0.05)	IRSF
56183.5	51.1	15.68(0.05)	14.39(0.04)	13.98(0.06)	IR Cam
56184.7	52.3	15.24(0.05)	14.33(0.03)	13.86(0.04)	IRSF
56185.7	53.3	15.22(0.05)	14.27(0.03)	13.83(0.05)	IRSF
56186.7	54.3	15.10(0.05)	14.29(0.03)	13.83(0.06)	IRSF
56189.8	57.4	15.38(0.04)	14.38(0.03)	13.78(0.03)	IRSF
56190.7	58.3	15.43(0.05)	14.39(0.02)	13.78(0.03)	IRSF
56192.7	60.3	15.43(0.05)	14.41(0.03)	13.81(0.03)	IRSF
56193.5	61.1	15.54(0.05)	...	...	IR Cam
56194.7	62.3	15.35(0.07)	14.40(0.03)	13.88(0.04)	IRSF
56195.7	63.3	15.59(0.06)	14.39(0.03)	13.80(0.05)	IRSF
56196.6	64.2	15.85(0.06)	14.60(0.03)	13.84(0.05)	NIC
56196.7	64.3	15.69(0.06)	14.52(0.03)	13.82(0.05)	IRSF
56199.7	67.3	15.62(0.06)	14.51(0.03)	13.83(0.04)	IRSF
56200.7	68.3	15.87(0.09)	14.50(0.04)	13.77(0.05)	IRSF
56201.5	69.1	...	14.44(0.07)	13.83(0.07)	IR Cam
56201.7	69.3	15.60(0.06)	14.53(0.04)	13.71(0.04)	IRSF
56202.5	70.1	...	14.80(0.05)	13.83(0.05)	IR Cam
56202.5	70.1	15.92(0.11)	14.70(0.03)	14.00(0.04)	NIC
56202.7	70.3	15.97(0.07)	14.69(0.04)	13.87(0.05)	IRSF
56203.8	71.4	15.77(0.05)	14.60(0.03)	13.84(0.03)	IRSF
56204.5	72.1	16.04(0.18)	14.91(0.04)	14.09(0.09)	NIC
56204.5	72.1	...	14.66(0.08)	13.78(0.06)	IR Cam
56205.5	73.1	...	...	13.96(0.06)	IR Cam
56205.7	73.3	15.79(0.07)	14.62(0.04)	13.80(0.04)	IRSF
56207.5	75.1	16.12(0.27)	14.83(0.03)	14.01(0.04)	NIC
56208.5	76.1	...	...	14.07(0.04)	IR Cam
56208.8	76.4	15.94(0.07)	14.68(0.04)	13.94(0.05)	IRSF
56210.4	78.0	...	...	14.95(0.09)	IR Cam
56211.5	79.1	...	14.81(0.05)	...	IR Cam
56211.8	79.4	16.22(0.08)	14.86(0.04)	13.91(0.04)	IRSF

Table 7. (Continued)

MJD	Phase	$J$	$H$	$K_s$	Instruments
56212.5	80.1	16.43(0.22)	15.00(0.10)	14.13(0.07)	NIC
56212.5	80.1	...	...	14.08(0.10)	IR Cam
56212.8	80.4	16.04(0.08)	14.84(0.05)	13.95(0.05)	IRSF
56213.9	81.5	16.13(0.07)	14.87(0.04)	14.01(0.05)	IRSF
56214.5	82.1	16.53(0.21)	15.19(0.12)	14.24(0.09)	NIC
56216.4	84.0	...	15.26(0.04)	14.34(0.07)	NIC
56220.4	88.0	...	15.13(0.11)	14.36(0.12)	IR Cam
56223.4	91.0	...	15.08(0.08)	14.33(0.08)	IR Cam
56225.8	93.4	16.71(0.11)	15.17(0.05)	14.26(0.06)	IRSF
56226.4	94.0	16.68(0.25)	15.60(0.05)	14.48(0.07)	NIC
56226.8	94.4	16.72(0.13)	15.29(0.06)	14.16(0.06)	IRSF
56227.8	95.4	16.59(0.17)	15.18(0.08)	14.21(0.10)	IRSF
56228.4	96.0	...	...	14.24(0.06)	IR Cam
56228.7	96.3	16.71(0.16)	15.40(0.08)	14.11(0.07)	IRSF
56231.8	99.4	16.81(0.10)	15.40(0.05)	14.26(0.04)	IRSF
56232.8	100.4	16.92(0.11)	15.50(0.05)	14.33(0.05)	IRSF
56233.8	101.4	16.95(0.14)	15.59(0.07)	14.35(0.06)	IRSF
56237.4	105.0	...	16.31(0.25)	15.13(0.37)	NIC
56238.7	106.3	17.50(0.25)	15.72(0.07)	14.40(0.06)	IRSF
56240.7	108.3	16.88(0.09)	15.62(0.05)	14.50(0.05)	IRSF
56241.7	109.3	17.03(0.11)	15.73(0.06)	14.53(0.05)	IRSF
56242.7	110.3	17.08(0.16)	15.83(0.09)	14.45(0.06)	IRSF
56242.7	110.3	17.08(0.16)	15.83(0.09)	14.45(0.06)	IRSF
56243.8	111.4	17.18(0.11)	15.73(0.06)	14.48(0.04)	IRSF
56243.8	111.4	17.18(0.11)	15.73(0.06)	14.48(0.04)	IRSF
56244.8	112.4	17.24(0.13)	15.74(0.06)	14.57(0.05)	IRSF
56244.8	112.4	17.24(0.13)	15.74(0.06)	14.57(0.05)	IRSF
56245.7	113.3	17.63(0.20)	15.80(0.05)	14.68(0.05)	IRSF
56246.7	114.3	17.11(0.14)	15.88(0.06)	14.55(0.05)	IRSF
56247.7	115.3	17.01(0.11)	15.81(0.05)	14.76(0.05)	IRSF
56248.7	116.3	17.24(0.14)	16.12(0.07)	14.78(0.06)	IRSF
56249.8	117.4	17.24(0.12)	15.89(0.06)	14.70(0.05)	IRSF
56250.7	118.3	17.24(0.12)	16.01(0.06)	14.75(0.05)	IRSF
56251.7	119.3	17.83(0.19)	16.14(0.07)	14.94(0.05)	IRSF
56257.8	125.4	...	15.96(0.09)	15.13(0.13)	IRSF
56259.8	127.4	...	16.70(0.25)	15.16(0.18)	IRSF
56264.8	132.4	...	16.38(0.12)	15.11(0.10)	IRSF
56267.8	135.4	...	16.77(0.13)	15.24(0.08)	IRSF
56268.8	136.4	...	16.51(0.11)	15.23(0.08)	IRSF
56269.8	137.4	...	16.34(0.12)	15.42(0.12)	IRSF
56272.8	140.4	...	16.80(0.17)	15.32(0.10)	IRSF
56348.1	215.7	> 19.05	> 20.82	> 19.39	IRSF

Table 8. Log of spectroscopic observations of SN 2012dn

MJD	Phase	Coverage	Resolutions	Instruments
56131.6	-0.8	4500-9000Å	15.0Å	HOWPol
56132.6	0.2	4500-9000Å	15.0Å	HOWPol
56133.7	1.3	4500-9000Å	15.0Å	HOWPol
56134.7	2.3	4500-9000Å	15.0Å	HOWPol
56137.5	5.1	4500-9000Å	15.0Å	HOWPol
56138.6	6.2	4500-9000Å	15.0Å	HOWPol
56139.6	7.2	4500-9000Å	15.0Å	HOWPol
56140.6	8.2	4500-9000Å	15.0Å	HOWPol
56141.6	9.2	4500-9000Å	15.0Å	HOWPol
56142.6	10.2	4500-9000Å	15.0Å	HOWPol
56143.6	11.2	4500-9000Å	15.0Å	HOWPol
56149.6	17.2	4500-9000Å	15.0Å	HOWPol
56150.5	18.1	4500-9000Å	15.0Å	HOWPol
56155.5	23.1	4500-9000Å	15.0Å	HOWPol
56156.5	24.1	4500-9000Å	15.0Å	HOWPol
56158.5	26.1	4500-9000Å	15.0Å	HOWPol
56159.6	27.2	4500-9000Å	15.0Å	HOWPol
56160.5	28.1	4500-9000Å	15.0Å	HOWPol
56163.6	31.2	4500-9000Å	15.0Å	HOWPol
56164.6	32.2	4500-9000Å	15.0Å	HOWPol
56165.6	33.2	4500-9000Å	15.0Å	HOWPol
56170.5	38.1	4500-9000Å	15.0Å	HOWPol
56172.5	40.1	4500-9000Å	15.0Å	HOWPol
56182.5	50.1	4500-9000Å	15.0Å	HOWPol
56183.5	51.1	4500-9000Å	15.0Å	HOWPol
56184.5	52.1	4500-9000Å	15.0Å	HOWPol
56193.5	61.1	4500-9000Å	15.0Å	HOWPol
56196.5	64.1	4500-9000Å	15.0Å	HOWPol
56197.4	65.0	4500-9000Å	15.0Å	HOWPol